



UNIVERSITY OF LEEDS

This is a repository copy of *Experimental and numerical study on wear characteristics of steel surfaces involving the tribochemistry of a fully formulated oil. Part II: Computational modelling.*

White Rose Research Online URL for this paper:

<https://eprints.whiterose.ac.uk/194408/>

Version: Accepted Version

---

**Article:**

Gong, Y, Wang, Y, Ghanbarzadeh, A [orcid.org/0000-0001-5058-4540](https://orcid.org/0000-0001-5058-4540) et al. (5 more authors) (2023) Experimental and numerical study on wear characteristics of steel surfaces involving the tribochemistry of a fully formulated oil. Part II: Computational modelling. *Tribology International*, 177. 107976. ISSN 0301-679X

<https://doi.org/10.1016/j.triboint.2022.107976>

---

© 2022, Elsevier. This manuscript version is made available under the CC-BY-NC-ND 4.0 license <http://creativecommons.org/licenses/by-nc-nd/4.0/>.

**Reuse**

This article is distributed under the terms of the Creative Commons Attribution-NonCommercial-NoDerivs (CC BY-NC-ND) licence. This licence only allows you to download this work and share it with others as long as you credit the authors, but you can't change the article in any way or use it commercially. More information and the full terms of the licence here: <https://creativecommons.org/licenses/>

**Takedown**

If you consider content in White Rose Research Online to be in breach of UK law, please notify us by emailing [eprints@whiterose.ac.uk](mailto:eprints@whiterose.ac.uk) including the URL of the record and the reason for the withdrawal request.



[eprints@whiterose.ac.uk](mailto:eprints@whiterose.ac.uk)  
<https://eprints.whiterose.ac.uk/>

# Experimental and Numerical Study on Wear Characteristics of Steel Surfaces Involving the Tribochemistry of a Fully Formulated Oil Part

## II: Computational Modelling

Yajing Gong<sup>a</sup>, Yuechang Wang<sup>a\*</sup>, Ali Ghanbarzadeh<sup>a\*</sup>, Chun Wang<sup>a</sup>, Akihito Ishihara<sup>b</sup>, Yukio Tamura<sup>b</sup>, Anne Neville<sup>a</sup>, Ardian Morina<sup>a</sup>

\* Corresponding author for [y.wang1@leeds.ac.uk](mailto:y.wang1@leeds.ac.uk) (Yuechang Wang); [a.ghanbarzadeh@leeds.ac.uk](mailto:a.ghanbarzadeh@leeds.ac.uk) (Ali Ghanbarzadeh)

<sup>a</sup> Institute of Functional Surfaces, School of Mechanical Engineering, University of Leeds, Leeds, LS2 9JT, United Kingdom

<sup>b</sup> Manufacturing Engineering Development Centre, Production Division, Komatsu Ltd., Osaka 573-1011, Japan

### Abstract:

Modelling wear characteristics involving the fully formulated oil (FFO) with its tribochemistry is challenging due to its complex chemical components. This paper developed a model to simulate the tribochemistry, wear, and sublayer stress for rough surfaces lubricated with a general FFO with similar recipes and properties or other functional surfaces. The tribochemistry model and the wear model when using FFO were developed based on the existing modelling studies of zinc dialkyldithiophosphate (ZDDP) and experimental results of FFO in Part (I) of this research series. The layered contact model was applied to simulate the sublayer stress under the influence of the real-time tribofilm growth for the first time and can expand the computational dimensions. In the wear model, by using the concept of conservation of mass, the wear process can be described as follows: the mass of iron lost in the substrate is equal to the mass of iron consumed in the tribochemical reaction, which supplements the removal part of the tribofilm. Considering the different forms of iron in the tribofilm and the substrate, a method was improved to transfer the atomic percentage of iron (Fe at.%) in the tribofilm measured by X-ray photoelectron spectroscopy (XPS) to the wear coefficient in the Archard's wear equation. The simulation results are consistent with the critical tribological experimental results of FFO, such as tribofilm growth and wear evolution. The model also successfully simulates that the tribofilm formation has a buffering effect on the contact, and the tribofilm growth is promoted by temperature and shear.

**Keywords:** Wear Model; Tribofilm; Layered Contact Model; Boundary Lubrication Modelling

## Nomenclature

$a_0$	Hertzian contact radius
$A_m$	Etching area
$C, D$	Constants relevant to the two reaction rates
$C_p^{u_z}, C_p^\sigma$	Influence coefficient (IC) matrix of displacement and stress
$E$	Elastic modulus
$h$	Tribofilm or layer thickness
$h'$	Larger thickness between the ball and the disc
$h_a, h_b$	Maximum thickness that the two-step tribochemical reactions can reach, respectively
$h_{balance}$	Balanced thickness
$h_c$	Threshold thickness when tribochemical wear occurs
$h_{max}$	Maximum tribofilm thickness
$h_r$	Removed thickness
$h_{wear}, w$	wear depth
$H_{film}, H_s$	Hardness of the tribofilm and the substrate
$\sqrt{J_2}$	Von Mises stress
$K_{steel}, K_{film}$	Mechanical and tribochemical wear coefficient
$K_p, K_i, K_d$	Constants in PID controller
$m_{Fe-comp}, m_{Fe-wear}$	Mass of iron removed in the surface layer of tribofilm, and iron lost in the substrate
$M, N$	Total discrete grid points
$p, P$	Normal pressure or force
$p_{max}$	Maximum Hertzian contact pressure
$q_x, q$	Traction force, shear stress
$R^2$	The goodness-of-fit
$S$	The gap between the two rough surfaces
$S_l$	Sliding distance
$S_z$	Height of roughness surface
$t$	Time
$\Delta t$	Characteristic time length
$t_0$	Delayed time of the latter reactions
$U_p$	Plastic deformation
$u_z$	Normal displacement
$\nu$	Poisson's ratio
$v_l$	The relative sliding speed of the two contacting surfaces
$V_{Fe-comp}, V_{Fe-wear}$	The iron volume contained in the removal part of tribofilm and lost in the substrate.
$V_r$	The removed volume of tribofilm
$W$	Load

$\eta_{Fe-Vol}$	The volume fraction of iron in the removed volume of tribofilm
$\eta_r$	The ratio of removed thickness over the current thickness
$\mu$	Friction coefficient
$\rho_{FeO/S} \cdot \rho_{steel}$	The density of iron compounds(sulphides or oxides) and iron (steel)
$\sigma$	Stress
$\Omega$	Real contact area
$\omega$	Normal rigid body approach

## 1 Introduction

Wear is undesirable for most machine applications. Reducing wear has always been one of the main concerns of the industry. In the mining industry, the replacement cost of parts due to wear accounts for about half of the total maintenance cost [1, 2]. Thus, understanding the wear mechanism and monitoring the wear process is essential to improve the machine's service life and reduce cost and energy consumption.

Wear usually occurs through interactions between asperities [3]. Under severe operating conditions, the fluid film cannot sustain the load, and asperities on the two surfaces will come into direct contact. Then, a tribofilm is formed on the surfaces, resulting in the change of surface topography and material properties that affect the friction and wear phenomena. Therefore, the wear process under lubricated conditions is not a simple mechanical process. It is often accompanied by physical and chemical reactions at the contact interface.

Archard's wear equation is one of the most widely used wear simulation models [4] and was developed based on Holm's work on sliding electrical contacts [5]. It was developed for adhesive sliding wear, but many experiments have shown that its mathematical form also applies to other forms of wear. For wear models involving tribochemistry, there are several works based on Archard's wear equation or similar forms. The common idea is to correlate the wear coefficient  $K$  in the equation to a parameter from the tribochemical reaction. Bosman and Schipper [6] correlated iron content in the zinc dialkyldithiophosphate (ZDDP) tribofilm to the wear loss parameter, equivalent to the wear coefficient  $K$  in Archard's wear equation. Ghanbarzadeh *et al.* [7] proposed a linear relationship between  $K$  and the tribofilm thickness obtained by the Mini Traction Machine with the Spacer Layer Imaging Method (MTM-SLIM). Similarly, Akchurin and Bosman [8] used a linear relationship between wear rate and tribofilm thickness. They applied the tribofilm growth equation based on atomic force microscopy (AFM) measurements to estimate the growth on a macroscopic scale. Although these models for ZDDP are important steppingstones for tribochemistry modelling in the boundary lubrication regime, they cannot be directly applied to the fully formulated oil (FFO) because the wear trend on the steel surface with FFO does not vary monotonously with temperature (or tribofilm thickness) as it does with ZDDP, as indicated by the experiments in Part (I) of this research. Due to the complexity of the tribochemical reactions that occurs between FFO and the contact surface, a general wear model involving tribochemistry that can take into account the chemistry of the tribofilm is still lacking.

Tribochemical reaction kinetics are highly important for film-forming additives such as ZDDP under boundary lubrication conditions, so a few kinetics models were developed to capture their behaviours. From the experimental results of FFO in Part (I) of this research [9], it can be seen that its tribofilm has similar growth trends to the ZDDP tribofilm. It is also evident that the main compositions of FFO tribofilm are phosphate and sulphides. Therefore, a similar model of the tribofilm growth kinetics based on the ZDDP experiments could be used to establish the interfacial reaction model for FFO. Based on the macroscopic experimental results, So and Lin [10] used the diffusion model to simulate the chemical reaction process of ZDDP. Fujita and Spikes [11] used MTM-SLIM to study the growth and removal of ZDDP tribofilm at different temperatures. Andersson *et al.* [12] developed a tribofilm growth model based on the Arrhenius equation and provided a method to update the hardness of asperities considering the tribofilm thickness. Ghanbarzadeh *et al.* [13], based on the works of Bulgarevich *et al.* [14] and Andersson *et al.* [12], developed a mechano-chemical model to describe the growth and removal of the tribofilm. Based on microscopic AFM experiments, Gosvami *et al.* [15] investigated the thickness of ZDDP tribofilm at different temperatures and contact pressures. They found that the growth rate fitted well with the stress-activated Arrhenius model. Subsequently, Dorgham *et al.* [16] further discussed the growth kinetics and reaction order of ZDDP and ashless DDP. Recently, Dominguez-Garcia *et al.* [17] proposed a mass balance-based model for the growth and removal of tribofilms, which can be extended to simulate friction coefficients and wear. In short, most existing models are based on experimental results to model the reaction kinetics for tribofilm growth. Some incorporated a contact model of homogenous rough surfaces for simulation.

However, experimental studies on the mechanical properties of ZDDP have shown that the hardness and elastic modulus of the tribofilm are different from those of the steel substrate [18-20]. With the development of materials science and coating technology, the presence of the layer has been reported to have a significant impact on the stress field, so it is relevant to extend the stress field from a two-dimensional surface to a three-dimensional layered problem [21]. In addition, the formation of ZDDP tribofilm may promote micropitting wear [22-27], which also indicates the need for subsurface stress calculations. Therefore, introducing a layered contact model can optimise the modelling framework for more applications. The general elastic theory for solving stress states and displacements on the layered system was originally developed by Burmister [28-30]. Further improvements to the layered contact models were developed by many researchers [21, 31-46]. O'Sullivan and King [21] used the least-square error method for a three-dimensional problem to calculate the normal and quasi-static sliding contact stress fields of a smooth rigid sphere in a layered elastic half-space. Nogi and Kato [44] used the conjugate gradient method and fast Fourier Transform to speed up the simulation and use it for real rough surfaces under normal loading. Following Tian and Bhushan [47], who applied the variational principle for computing elastic-perfectly plastic problems for homogenous materials, Peng and Bhushan extended the method to layered rough surfaces under dry and wet conditions [41] or sliding conditions [42, 43]. At the same time, the development of numerical methods has also optimised the solution of layered contact problems, such as the semi-analytical method [21, 28-32], the finite element method [33-38], and the boundary element method [39-43]. In addition to the above-mentioned layered contact models with fully-

bonded interfaces, many layered models with different interfacial boundary conditions have been proposed, such as spring-like [48, 49], dislocation-like [50-52], force-like [52, 53], and frictionless contact interface [52, 54, 55]. The development of diverse layered contact models provides a solid theoretical foundation for the modelling work in this paper. Meanwhile, to the best of our knowledge, there is little research on the joint modelling of the layered contact model integrated with the effect of tribochemistry and wear.

This paper aims to develop a wear model involving the tribochemistry of FFO, mainly containing ZDDP, detergents, and the dispersant under the boundary lubrication regime. This paper applies a layered contact model for the rough surfaces to simulate the wear and subsurface stress distribution under the influence of the FFO tribofilm. The simulation results are compared with the experimental results of the tribofilm growth and wear evolution at different temperatures presented in Part (I) [9] for validation purposes. The stress distributions with the effect of the tribofilm are discussed as well.

## 2 Modelling Framework

Since the whole modelling work contains multidisciplinary theories, numerical methods, and the data exchange between simulation and experiments, the framework of the model is first explained for better understanding, as shown in Fig. 1. It is worth mentioning that the experiments in Part (I) of this research series were designed under boundary lubrication conditions and the effect of fluid viscosity on the wear trend with temperature was also excluded experimentally, so the elastohydrodynamic lubrication simulation was not considered in the modelling framework of this work. The framework consists of five parts, surface topography, layered contact algorithm, tribochemistry model, wear model, and stress distribution. Firstly, two random rough surfaces are numerically generated, representing the surfaces of a ball and a disc. These surfaces are the inputs to the model with the same working conditions and material properties as those used in Part (I) of this research. Then, a layered contact algorithm solves the pressure distribution and elasto-plastic deformation between the two rough surfaces. Next, the tribofilm thickness is calculated by the tribochemistry model developed from the previous modelling works on ZDDP in literature and from the experimental results of FFO in Part (I). Wear is calculated by Archard's wear equation in which wear coefficient  $K$  is correlated to the tribofilm thickness using the atomic percentage of iron (Fe at.%) in the tribofilm obtained by X-ray photoelectron spectroscopy (XPS) analysis. In addition, stress distribution under the real-time growing tribofilm can also be calculated based on the layered contact model. If the traction is considered, the friction coefficients from tribo-tests are input into the model to simulate the stress at different temperatures.

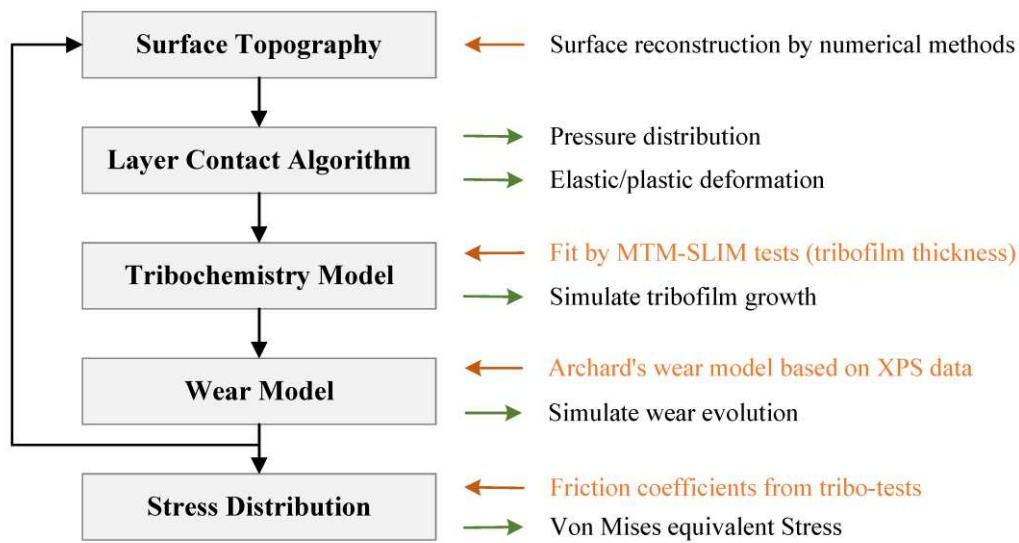


Fig. 1 Framework of the model to solve tribochemistry, wear behaviour, and stress based on layered contact model for rough surfaces. (The parts involving the experimental results of FFO in Part (I) of this study series are explained in orange text. The orange and green arrows represent the critical input and output into the simulation, respectively).

Since the modelling framework for simulating tribochemistry and wear are relatively similar [7, 8], it is necessary to point out the critical modifications and improvements of the modelling work in this paper.

- 1) A layered contact algorithm is used to extend the simulation of wear and tribochemistry from the conventional two-dimensional rough surface to a three-dimensional layered case.
- 2) The tribofilm with a certain thickness is treated as one layer to more realistically represent the contact state after the change in surface material properties due to the formation of the tribofilm.
- 3) The tribochemistry model is modified based on the stress-activated Arrhenius equation for ZDDP and experimental results of FFO.
- 4) The wear model is based on Archard's wear equation. A method is proposed to calculate the wear coefficient from the Fe at.% in the tribofilm measure by XPS. The different chemical structures of iron in the tribofilm and the substrate are considered in the model.
- 5) In addition, stress distributions are simulated under different temperatures, tribofilm thickness, and friction coefficients.

### 3 Theory and Numerical Methods

#### 3.1 Solutions to Elasto-plastic Contact Problem

According to the theory of contact mechanics [56], the general boundary constraints for dry contact problems need to satisfy two conditions at the same time.

$$S(x, y) + \omega = S_{zi}(x, y) + u_z(x, y) \quad (1)$$

$$W = \int_{\Omega} p(x, y) d\Omega \quad (2)$$

where  $S_{zi}$  is the initial asperity height;  $S$  is the gap between the two rough surfaces;  $\omega$  is the normal rigid body approach, and  $u_z$  is the displacement in the  $z$ -direction.

In addition, the relationship between the surface gap  $S$  and pressure  $p$  at a point  $(x, y)$  should satisfy the following conditions.

$$\begin{cases} S(x, y) = 0, & p(x, y) > 0, & (x, y) \in \Omega \\ S(x, y) > 0, & p(x, y) = 0, & (x, y) \notin \Omega \end{cases} \quad (3)$$

The layered contact problem can be described as a rigid ball pressed against a layered solid, which is an elastic half-space (substrate) bonded with a layer of thickness  $h$ , as shown in Fig. 2a. The normal force is  $W$ . It induces a tangential force  $\mu W$ , where  $\mu$  is the friction coefficient. The layer thickness is negligible compared to the thickness of the elastic half-space. The interface between the layer and the substrate is fully bonded without slipping or lifting. The tangential displacement on the surface is neglected, so the contact is frictionless. The contact between the ball and the layer is microscopically regarded as a contact between asperities within a nominal contact domain  $\Omega$ . When two asperities come into contact at a point  $(x, y)$ , the normal pressure between them is denoted as  $p(x, y)$ , accompanied by the traction stress  $q(x, y) = \mu p(x, y)$ , as shown in Fig. 2b.

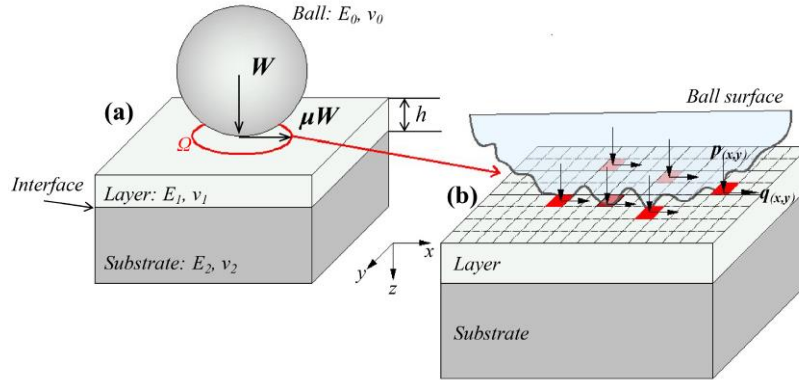


Fig. 2 Schematic diagram of (a) a rigid ball in contact with a layered solid and (b) the real contact between asperities in the nominal contact area  $\Omega$ .

Peng and Bhushan [41] applied the variational principle to solve the elasto-plastic contact problems for layered materials with rough surfaces. For a layered solid, the displacement/stress response induced by a unit pressure excitation can be described by the influence coefficient (IC) matrix, denoted as  $C_{\text{subscript}}^{\text{superscript}}$ . The superscript is  $u_z$  or  $\sigma$ , which represents the IC matrix for normal displacement or stress, respectively. The subscript is  $p$  or  $q_x$ , which represents the IC matrix excited by the normal pressure or the tangential traction at

the  $x$ -direction. For example, the IC matrix  $C_{p_j}^{u_z}$  is the normal displacement in  $z$ -direction induced by a unit pressure  $p$ .

O'Sullivan and King [21] used the harmonic functions of Papkovitch-Neuber ( $P$ - $N$ ) elastic potentials  $\phi_0$  and  $\vec{\phi}=(\phi_1, \phi_2, \phi_3)$  to directly obtain the explicit expression of the IC matrix in the frequency domain, called the frequency response function (FRF). The derivations are expressed in Appendix A for brevity. After obtaining the expressions of FRFs for displacement and stress, the discrete convolution and fast Fourier transform method proposed by Liu *et al.* [57] is used to calculate the deformation or the stress components in the time domain. The product of the deformation/stress components of FRFs and the pressure matrix after the fast Fourier transform is calculated first, followed by the inverse fast Fourier transform. The process can be summarised in Equ. (4) where the symbol hat “^” means the corresponding Fourier transform of the matrix. The inverse Fourier transform is denoted as  $\mathfrak{F}^{-1}$ .

$$\mathbf{u}_z = \mathbf{C}_p^{u_z} \otimes \mathbf{p} + \mathbf{C}_{q_x}^{u_z} \otimes \mathbf{q}_x = \mathfrak{F}^{-1} \left[ \hat{\mathbf{C}}_p^{u_z} \cdot \hat{\mathbf{p}} + \hat{\mathbf{C}}_{q_x}^{u_z} \cdot \hat{\mathbf{q}}_x \right] \quad (4)$$

$$\boldsymbol{\sigma}_{ij} = \mathbf{C}_p^{\sigma_{ij}} \otimes \mathbf{p} + \mathbf{C}_{q_x}^{\sigma_{ij}} \otimes \mathbf{q}_x = \mathfrak{F}^{-1} \left[ \hat{\mathbf{C}}_p^{\sigma_{ij}} \cdot \hat{\mathbf{p}} + \hat{\mathbf{C}}_{q_x}^{\sigma_{ij}} \cdot \hat{\mathbf{q}}_x \right] \quad (i \text{ and } j = x, y, z) \quad (5)$$

Liu and Wang [58] further improved the efficiency and accuracy of the conversion from FRF to IC matrix by multiplying the FRF by a shape function of a rectangular pulse to obtain the continuous IC matrix. To avoid the singularity of the IC matrix at the origin ( $m=0, n=0$ ), a 64-Gaussian quadrature integration is used to estimate the value [44].

Firstly, the frictionless contact problem on the layer surface is solved. Since the normal displacement caused by the surface shear traction is much smaller than the effect of normal pressure [56, 59], the friction coefficient is set to zero when solving the displacement in Equ. (4). The iteration method to solve the contact problem in Equ. (1)-(4) used in the paper was proposed by Stanley and Kato [60]. The plastic deformation is considered by using the method proposed by Almqvist *et al.* [61] for the elastic-perfectly plastic material. Then, the effect of tangential traction is added through the friction coefficient in the stress calculation.

In the iteration procedure, adjusting the rigid gap between the two contact surfaces determines the accuracy and speed of the pressure convergence, which is also the key step in adjusting the load balance. The Proportional-Integral-Differential (PID) controller proposed by Wang *et al.* [62] was applied to speed up this process. The discrete algorithm of the PID controller for pressure adjustment is expressed as:

$$p_{n+1} = p_n + \Delta p = p_n + (K_p e_n + K_i \sum_{j=0}^n e_j + K_d [e_n - e_{n-1}]) \quad (6)$$

where  $e_n = W - W_n$  is the difference between the targeted normal load  $W$  and the sum of the pressures  $W_n$  (Equ. (2)) in the  $n^{\text{th}}$  iteration;  $K_p$ ,  $K_i$  and  $K_d$  are constants.

For stress analysis, von Mises stress  $\sqrt{J_2}$  is usually used as equivalent stress in elastoplastic mechanics to determine the material yielding [56], which is calculated by:

$$\sqrt{J_2} = \sqrt{\frac{1}{2} \left[ (\sigma_{xx} - \sigma_{yy})^2 + (\sigma_{yy} - \sigma_{zz})^2 + (\sigma_{zz} - \sigma_{xx})^2 \right] + 3(\sigma_{xy}^2 + \sigma_{yz}^2 + \sigma_{zx}^2)} \quad (7)$$

The algorithm of the layered contact model was coded by the authors using MATLAB software. Model validation was performed using the same parameters provided in the O'Sullivan and King paper [21], and the simulation results in this work were consistent with those in the literature. For brevity, the results are shown in Supplementary Material.

### 3.2 Tribofilm Growth Model for FFO

According to the experimental results in Part (I) of this research, the tribofilm growth process of FFO exhibits many similarities to that of ZDDP. The difference is that there is a process of thickness reduction and re-growth for FFO after a certain stage of tribofilm growth, which is evident at test times of 30 mins to 60 mins at 80 °C and 100 °C. It is assumed that two tribochemical reaction rates exist and that there may be a time difference between them.

Following the modelling work of Ghanbarzadeh *et al.* [7, 13] for ZDDP tribofilm, by analogy with the tribofilm thickness as a function of time and the fitting process of experimental results, the expression for the tribofilm thickness of FFO is described by Equ. (8).

$$h = h_a(1 - e^{-Ct}) + h_b(1 - e^{-D(t-t_0)}) \quad (8)$$

where  $h_a$  and  $h_b$  are the maximum thickness that can be achieved by the two-step tribochemical, respectively;  $t_0$  is the delayed time of the latter reactions;  $C$  and  $D$  are the constants relevant to the rates of the two reactions, respectively.

The curve-fitting Tool in MATLAB is used to fit the tribofilm growth curves at the four temperatures in Part (I) to obtain the constants in Equ. (8) and the fitting results are shown in Fig. 3. The  $R^2$  (goodness-of-fit) values for each curve are calculated automatically by MATLAB. The closer the  $R^2$  value is to 1, the better the fit of the regression line to the observed value. The fitting results without and considering the secondary growth at the four temperatures are shown in Fig. 3a and 3b, respectively. By comparing the values of  $R^2$ , the fitting results can better capture the reduction and re-formation of the tribofilm at 80 °C and 100 °C when a delayed time of the second tribofilm growth process is considered, and the proper delayed time is  $t_0 = 0.5$  (h). Thus, the equation considering the time difference  $t_0 = 0.5$  is applied in the simulation. The other four parameters in Equ. (8) at different temperatures are listed in Table 1.

The equation of tribofilm thickness should include two parts growth and removal. In the growth phase of the tribofilm, the growth is greater than the removal, while in the equilibrium phase, the growth and removal

reach a dynamic balance. In previous modelling works, the removal rate of tribofilm thickness was assumed to be a constant [17], linearly [8], or exponentially [7] proportional to the current tribofilm thickness. However, in this case of FFO, the removal amount of tribofilm cannot be measured in the tribotests alone, so the tribofilm thickness can be regarded as the net thickness that combines the growth and removal of the tribofilm.

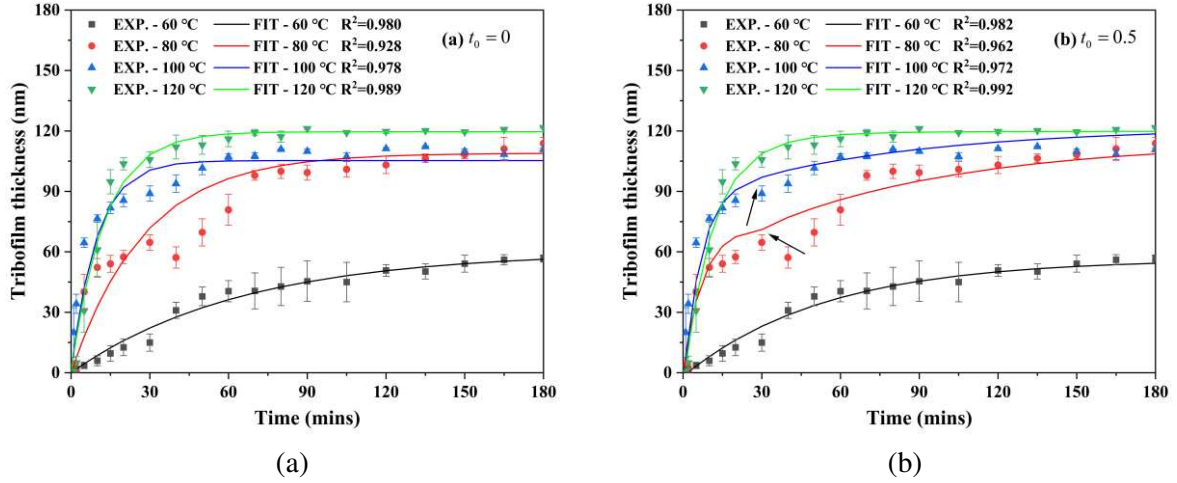


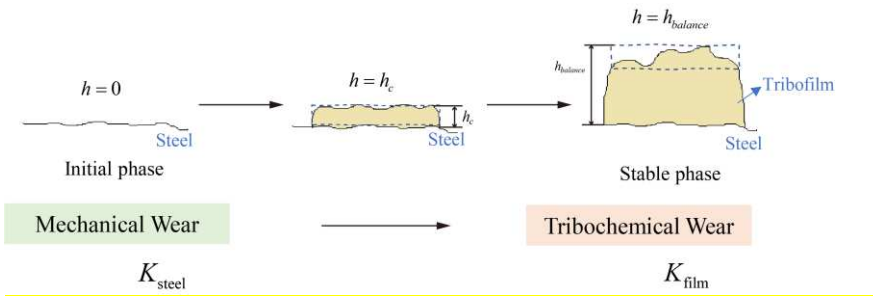
Fig. 3 Comparisons between fitting results and experimental results, (a)  $t_0 = 0$ , (b)  $t_0 = 0.5$

Table 1 The values of four parameters in the tribofilm growth equation Equ. (8) obtained by fitting the experimental results of tribofilm thickness as the function of time at different temperatures (Units:  $t, t_0$  – hour;  $h_a, h_b$  – nm;  $C, D$  – hour<sup>-1</sup>).

Temperatures	60 °C	80 °C	100 °C	120 °C
$h_a$	53.66	72.32	97.68	115.7
$C$	1.122	8.1	9.94	5.655
$h_b$	2.691	42.45	24.18	4.116
$D$	1.051	0.773	0.7927	2.287

### 3.3 Wear Model for FFO

According to the loss of the substrate material, the wear process on the steel surface when using FFO can be mainly divided into two stages, namely mechanical wear and tribochemical wear, as shown in Fig. 4. In the early stage of the rubbing process, tribofilm has not grown enough to cover the steel surface. Hence, the mechanical wear between the metal surfaces dominates. The wear coefficient  $K$  in Archard's wear equation is the wear rate of the steel-steel contact ( $K_{steel}$ ), which is about  $10^{-5} \sim 10^{-6}$  [63]. When the tribofilm grows to a thickness of  $h_c$ , it is assumed that there is almost no direct contact between the two metal surfaces. The wear under such conditions could be due to the continuous formation and removal of the tribofilm and the tribochemical reactions, so the wear coefficient is related to the thickness and composition of the tribofilm. The wear coefficient in the tribochemical wear stage is denoted as  $K_{film}$ .



**Fig. 4** The description of the wear process on the steel surface when using FFO.

Again, the formation of the tribofilm is a balance between growth and removal. Bosman and Schipper [6] considered that during the rubbing process, part of the surface layer of the tribofilm is removed. Then, to restore the chemical equilibrium of the tribofilm, the substrate interacts with additives through the tribochemical reactions to supplement the removed tribofilm, resulting in wear. When the removal volume of the tribofilm is known, the amount of substrate material contained in it can be calculated from Fe at.% measured by XPS analysis and correlated with the wear coefficient.

The same idea is applied to calculate the wear coefficient of the FFO tribofilm. However, the chemical analysis of the FFO tribofilm showed that the structure and density of iron in the FFO tribofilm differ from those in the substrate. Thus, wear is calculated by the material loss of the steel substrate resulting from the removal of the tribofilm. It should be highlighted that the concept of mass conservation of iron, rather than volume equivalence, is used in this work. First, the volume of iron in the removal part of the FFO tribofilm is calculated based on the XPS data and some assumptions. Then, the mass of iron in this part of the tribofilm is calculated from the density of iron sulphides/oxides. This mass equals the mass of iron lost in the steel substrate to restore chemical equilibrium. Next, the wear volume of the substrate can be calculated according to the density of steel. Finally, the wear coefficient  $K_{film}$  for the tribochemical wear process can be obtained through Archard's wear equation. The calculation procedure is described in detail as follows.

Fig. 5(a-d) shows the XPS depth profiling analysis of Fe at.% at four temperatures when tribofilm thickness reaches the stable phase. According to the relative atomic radius of iron, the volumetric percentages of iron (Fe vol.%) per unit depth can be calculated from Fig. 5(a~d) and fitted by a third-order polynomial, as shown in Fig. 5e. The  $h_{balance}$  represents the average thickness at the stable phase. The parameters in the polynomial fit results at different temperatures are shown in

**Table 2.** It is assumed that at the same temperature, the distribution of Fe atoms in the tribofilm along the depth is the same in the tribochemical wear stage. Then, when the tribofilm thickness is known, the iron volume in the tribofilm can be calculated from the Fe vol.% per unit depth in Fig. 5e.

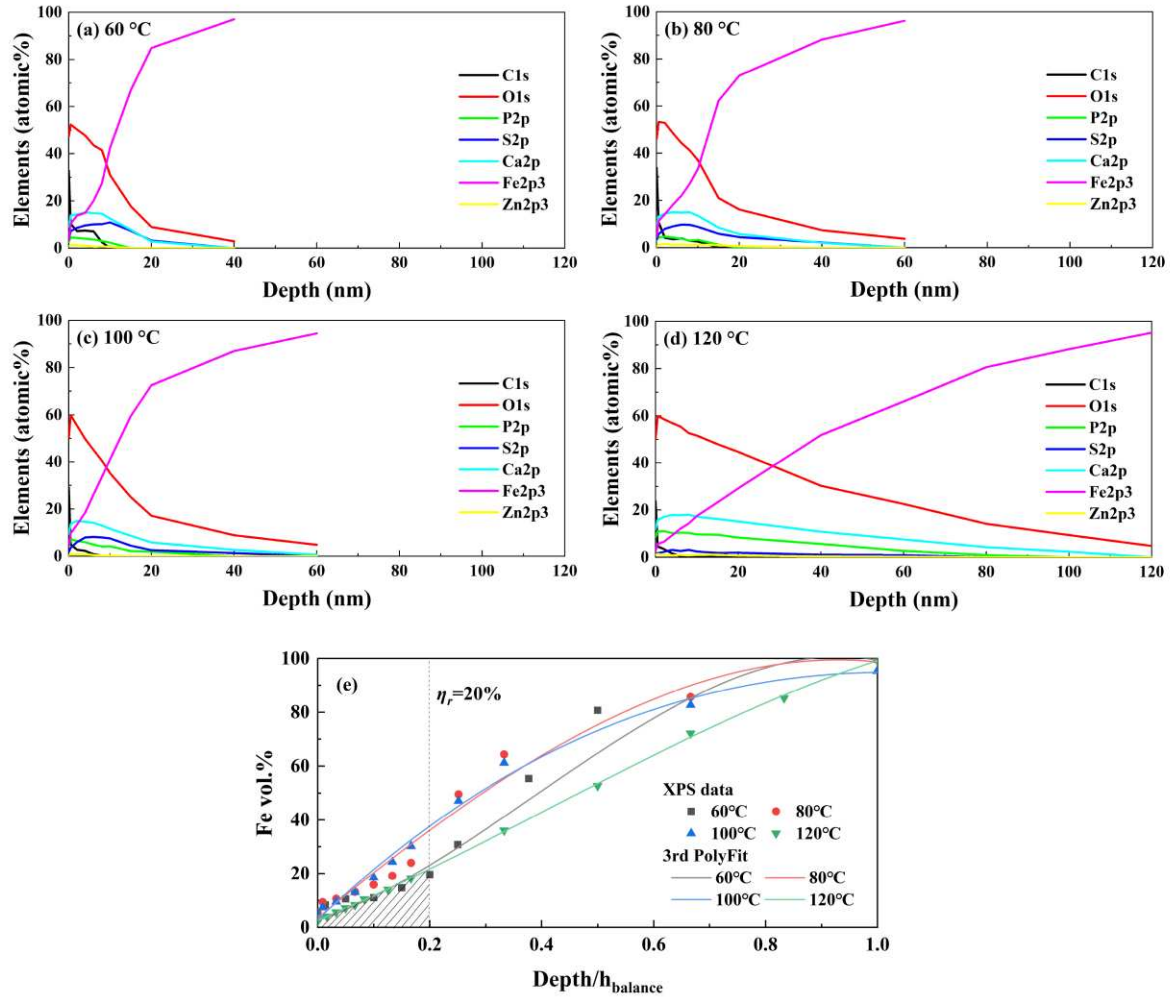


Fig. 5 The XPS depth profiling analysis of Fe vol.% at (a) 60 °C, (b) 80 °C, (c) 100 °C, (d)120 °C and (e) the 3rd polynomial fitting curves at different temperatures.

Table 2 The parameters in the 3rd polynomial fitting of the Fe vol.% as the function of the unit depth at different temperatures. (Function:  $y = p_1x^3 + p_2x^2 + p_3x + p_4$ ,  $y - Fe \text{ vol.}\%$ ;  $x - Depth/h_{balance}$ )

Temperature	60 °C	80 °C	100 °C	120 °C
$p_1$	-159.4	-39.23	17.67	-39.47
$p_2$	183.6	-38.18	-123.8	48.85
$p_3$	72.63	172.7	198.1	87.17
$p_4$	2.503	3.424	2.87	2.635

The thickness removed is unknown from experiments. Assuming that the removal rate of the tribofilm is constant in the tribochemical wear stage, denoted as  $\eta_r$  (see Fig. 5e). Then, for a certain thickness  $h$  ( $h \geq h_c$ ), the thickness of the tribofilm removed at the surface  $h_r$  can be calculated by

$$h_r = \eta_r \cdot h \quad (9)$$

So, the removal volume of the tribofilm at the surface layer is

$$V_r = h_r \cdot A_m \quad (10)$$

where  $A_m$  is the measurement area during the etching process.

As shown in Fig. 5e, taking 120 °C as an example, after integrating the shaded area and normalising the area, the volume fraction of iron  $\eta_{Fe-Vol}$  in the removed volume of the tribofilm can be obtained. Then, the volume of iron  $V_{Fe-comp}$  contained in the removal part of the tribofilm is calculated as:

$$V_{Fe-comp} = \eta_{Fe-Vol} \cdot V_r \quad (11)$$

According to the chemical analysis of tribofilm by Raman and XPS, Fe mainly exists in iron sulphides or iron oxides in the tribofilm. Hence, the density of iron compounds is the average density of these two, which is about  $\rho_{FeO/S} = 5 \text{ g/cm}^3$ .

Then, the mass of iron removed in tribofilm can be calculated by

$$m_{Fe-comp} = \rho_{FeO/S} \cdot V_{Fe-comp} \quad (12)$$

When tribofilm reaches a critical thickness  $h_c$ , it is considered that the wear in the substrate is mainly dominated by the tribochemical reactions, so the mass of iron removed in the surface layer of the tribofilm is equal to that lost in the substrate, that is

$$m_{Fe-wear} = m_{Fe-comp} \quad (13)$$

In the substrate, the density of iron is  $\rho_{steel} = 7.81 \text{ g/cm}^3$ . Therefore, the wear volume is

$$V_{Fe-wear} = m_{Fe-wear} / \rho_{steel} \quad (14)$$

The average wear coefficient  $K_{film}$  at the current thickness can be calculated by Archard's wear equation.

$$K_{film} = \frac{V_{Fe-wear} \cdot H_{film}}{P \cdot S_l} \quad (15)$$

where  $H_{film}$  is the hardness of the tribofilm;  $P$  is the normal load;  $S_l$  is the sliding distance (= sliding speed x time).

Finally, the wear depth at a contact point  $(x, y)$  can be calculated using Equ. (16).

$$h_{wear} = K_{film} \cdot P(x, y) v_l \Delta t / H(x, y) \quad (16)$$

where  $v_l$  is the relative sliding speed of the two contact surfaces;  $\Delta t$  is the characteristic time length;  $P(x, y)$  and  $H(x, y)$  are the pressure and hardness at the contact point, which can be obtained in the contact algorithm and hardness update, respectively.

### 3.4 Hardness Update Considering Plastic Deformation

Andersson *et al.* [12] developed a semi-deterministic chemo-mechanical model of the tribofilm that considered the variation of plastic deformation pressure with tribofilm thickness and plastic deformation depth. The plastic deformation pressure here can be regarded as the indentation hardness of the tribofilm, which is assumed to change linearly with the thickness. When the tribofilm has the maximum thickness, the hardness of the tribofilm is the minimum.

The relationship between the hardness  $H$  at the contact point  $(x, y)$ , tribofilm thickness, and plastic deformation of the two contact surfaces in the computational domain is expressed in Equ. (17).

$$H(x, y) = \begin{cases} H_s - \frac{H_s - H_{film}}{h_{max}}(h' - U_p) & \text{if } U_p < |h_1 - h_2| \\ H_s - \frac{H_s - H_{film}}{h_{max}}(h_1 + h_2 - U_p) & \text{if } |h_1 - h_2| \leq U_p \leq h_1 + h_2 \\ H_s & \text{if } h_1 + h_2 \leq U_p \end{cases} \quad (17)$$

where  $H_s$  and  $H_{film}$  are the hardness of the substrate and the balanced tribofilm, respectively;  $h_{max}$  is the maximum tribofilm thickness;  $U_p$  is the plastic deformation;  $h_1$  and  $h_2$  are the tribofilm thickness of the two rubbing bodies at the contact point, respectively;  $h'$  is the larger thickness between  $h_1$  and  $h_2$ .

Many studies have shown that the mechanical properties of the ZDDP tribofilm will be influenced by the temperatures and the chemical compositions of the tribofilm. The chemical compositions of the FFO tribofilm are similar to those of the ZDDP tribofilm, where phosphates and sulphides are the main components. Thus, the mechanical properties of FFO tribofilm can be estimated by ZDDP tribofilm.

Akchurin and Bosman combined the empirical variation of hardness with tribofilm thickness and the compensation factor as a function of temperature to calculate the tribofilm hardness  $H_{film}$  at different temperatures [6, 8]. When FFO is used, the same curves in the reference are applied to estimate the hardness of the tribofilm in Equ. (15) at four test temperatures by curve-fitting and interpolation method. The results are listed in Table 3.

Table 3 The hardness of FFO tribofilm at different temperatures, estimated by the empirical curve of hardness as the function of the thickness and the compensation factor.

Temperatures	60 °C	80 °C	100 °C	120°C
Thickness	60 nm	110 nm	115 nm	120 nm
Compensation factor	0.716	0.563	0.407	0.297
$H_{film}$	2.1 GPa	1.5 GPa	1.1 GPa	0.77 GPa

Although it is known that the elastic modulus of ZDDP tribofilm varies with hardness [18-20], the average elastic modulus of the tribofilm is set to be 85 GPa in the simulation temperatures to simplify the first simulation for FFO.

### 3.5 Simulation Procedure

The flowchart for simulating tribofilm thickness, wear, and stress is illustrated in Fig. 6. The material properties and working conditions in the input parameters are mainly determined by experimental results of FFO in Part (I) of this research series, as listed in Table 4. All the simulations were performed by MATLAB (version 2019b).

Table 4 Input Parameters in the simulation.

Parameters	
Ball Roughness	20 nm
Disc Roughness	10 nm
Elastic Modulus – Steel	210 GPa
Elastic Modulus – Tribofilm	85 GPa
Poisson’s Ratio – Steel	0.3
Poisson’s Ratio – Tribofilm	0.3
Hardness – Steel	8 GPa
Wear Coefficient $K_{steel}$	$10^{-5}$
Entrainment Speed	0.1 m/s
Max Hertzian Pressure	1.15 GPa
Slide-to-Roll Ratio (SRR)	150 %

In this work, simulated rough surfaces are used in the simulation. Two Gaussian rough surfaces were generated by Hu and Tonder’s method [64] to represent the ball and disc surfaces, respectively, as shown in Fig. 7. The computational domain is  $[-6a_0 < x < 6a_0, -6a_0 < y < 6a_0]$ , where  $a_0$  is the Hertzian contact radius. The number of nodes is 129x129 to balance the computing time and a large number of loading cycles.

At the beginning of the simulation, both the initial material of the ball and the disc are set to be steel, that is  $E_{layer} = E_{substrate} = E_{steel}$ , which is equivalent to the simulation of homogeneous steel material. The updated hardness and the tribofilm thickness are calculated by Equ. (17) and Equ. (8), respectively. The wear coefficient  $K$  in Equ. (16) is  $K_{steel}$ .

After several time steps of the calculation, the tribofilm can be considered a continuous layer when the average tribofilm thickness on the ball surface or the disc surface in the contact area is larger than its initial surface roughness ( $R_q$ ). Then, the elastic modulus of the layer changes to the tribofilm’s modulus  $E_{layer} = E_{tribofilm}$ , so the contact solid is changed to the steel substrate with a tribofilm layer. The layer thickness

is updated to the average thickness of the tribofilm at this step. The IC matrix in the layered contact model is re-calculated. The deformation and contact pressure will be updated correspondingly with the new material parameters for the contact calculation in the next time step.

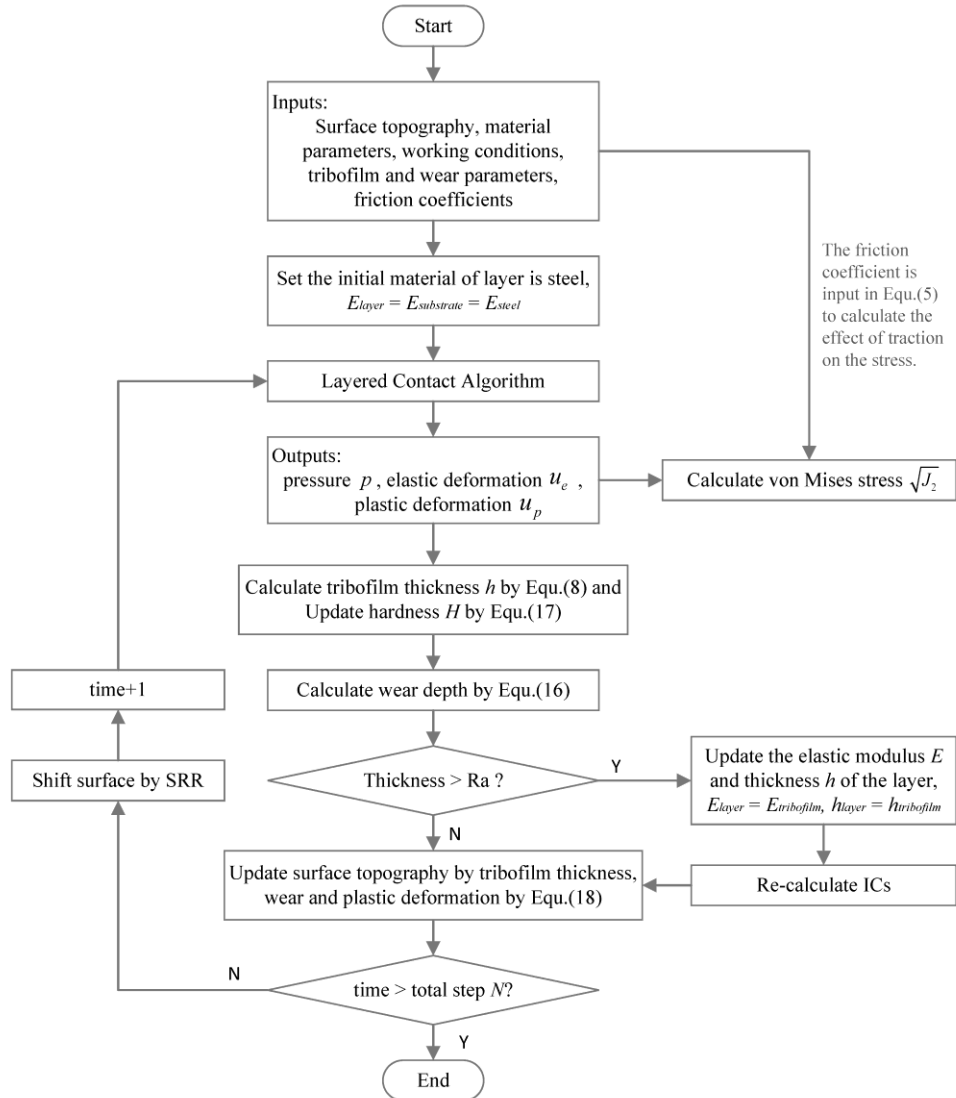


Fig. 6 Flowchart for simulating the tribofilm growth, wear, and stress.

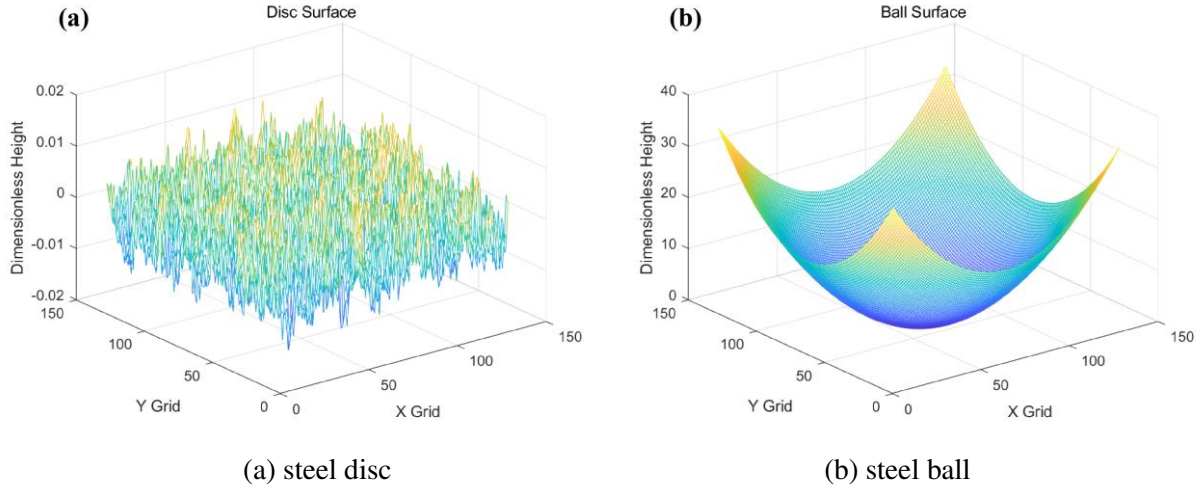


Fig. 7 The generated surfaces of (a) the steel disc and (b) the steel ball by MATLAB.

At each time step, the surface topography of the ball and the disc will be changed by tribofilm thickness, wear, and plastic deformation, which can be described in Equ. (18).

$$\begin{cases} S_{z1}^{n+1} = S_{z1}^n + 0.5 \times U_p^n - h_1^n + w_1^n \\ S_{z2}^{n+1} = S_{z2}^n - 0.5 \times U_p^n + h_2^n - w_2^n \end{cases} \quad (18)$$

where the number 1 and 2 in the subscript represent the ball surface and the disc surface, respectively;  $S_z$  is the rough surface;  $h$  is the tribofilm thickness;  $w$  is the wear depth;  $n$  is the  $n^{\text{th}}$  time step.

For the SRR shifting, since the contact area is fixed at the centre of the computational domain, rolling and sliding between surfaces and wear need to be realised by moving the two rough surface matrices. 1) Rolling. In each time step, both the two rough surfaces are moved one node along the sliding direction, such as the point  $(i, j) \rightarrow (i+1, j)$ . 2) Sliding: When the step number  $n$  is divisible by  $1/SRR$ , one of the surfaces adds one additional movement of a node, such as a point  $(i, j) \rightarrow (i+2, j)$ . The other surface keeps one node's movement. Finally, the stress distribution of the ball and the disc can be simulated.

## 4 Results and Discussions

### 4.1 Tribofilm Thickness and Wear

Fig. 8 shows the simulation and experimental results of FFO tribofilm growth at different temperatures. By comparison, the simulation results are consistent with the experimental results. This is also in accordance with the increase of the balanced thickness of the tribofilm with increasing temperature. The simulated tribofilm growth curves at 80 °C and 100 °C in the stable phase also show similar fluctuations to the experimental results, which may be caused by the increase in wear.

Fig. 9 compares the simulation and experimental results of the average wear depth on the disc. In the wear mechanism involving the tribochemistry of FFO, the initial wear stage is considered to occur only between steel and steel. When the tribofilm reaches a specific thickness  $h_c$ , only tribochemical wear is considered to occur. Therefore, the results of the wear simulations at the four temperatures show that the initial wear rate is significant, but the wear depths are almost the same. However, when the tribofilm thickness reaches  $h_c$ , the wear rate begins to decrease and matches well with the wear slope of the experimental results at all temperatures. The thickness  $h_c$  in the simulation is 1.4, 2.2, 2.4, and 2.5 times the maximum removed thickness at 60, 80, 100, and 120 °C, respectively. This multiple is basically in line with the ratio of the balanced tribofilm thickness at different temperatures. Although the higher the temperature, the higher the transition thickness  $h_c$  at which tribochemical wear occurs. However, since temperature also accelerates the growth rate of the tribofilm, excessive mechanical wear due to increased thickness will not occur at higher temperatures, as shown in Fig. 9.

In short, this model achieves simulation results of tribofilm thickness and wear in general agreement with the corresponding experimental results of FFO.

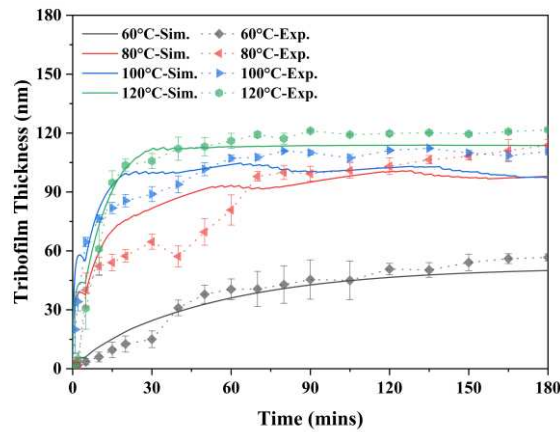


Fig. 8 Comparisons between the experimental results and simulation results of tribofilm thickness on the ball at different temperatures.

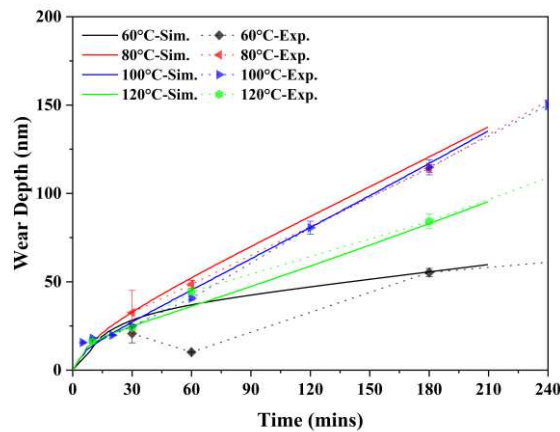


Fig. 9 Comparisons between the experimental results and simulation results of wear depth on the disc at different temperatures.

## 4.2 Stress Distribution

The tribofilm is regarded as a surface layer covering the steel substrate, so the contact state is different after the change in material properties and thickness of the surface layer, which also affects the stress in the sublayer. In addition, considering the differences in friction coefficients at different temperatures, the average friction coefficients when the tribofilm reaches the stable phase are calculated and used in the stress calculation listed in Table 5.

Table 5 Friction coefficients in the stress calculation at different temperatures.

Temperatures	60 °C	80 °C	100 °C	120 °C
Friction Coefficient	0.108	0.122	0.124	0.132

### 4.2.1 Von Mises Stress

Fig. 10 shows the von Mises stress at a cross-section of  $y = 0$  at different temperatures, corresponding to experimental time steps of 30 mins and 180 mins. The  $x$ -axis and stress are dimensionless;  $a_0$  is the Hertzian contact radius;  $p_{\max}$  is the maximum Hertzian contact pressure. The  $z$ -axis is the real value of depth that can directly show the tribofilm thickness (pointed out by arrow), and the positions of the maximum dimensionless stress are highlighted with value.

At all test temperatures, the maximum stress occurs at the interface of the tribofilm/substrate. The maximum stress decreases slightly as the test time increases. This may be due to an increase in contact area or the tribofilm thickness, which reduces the contact pressure. The maximum stress values at the four temperatures have little difference at the same test time, but in comparison, there is a minimum value at 80 °C (Fig. 10b and 10f). This may be due to the poor durability of tribofilm at 80 °C, so it is still easy to be removed even if it suffers from lower stress. Meanwhile, more iron is consumed in the tribochemical reaction that complements the tribofilm, resulting in increased wear at this temperature. This also suggests that the wear mechanism when using FFO is related to pathways and products of tribochemical reactions.

### 4.2.2 Interfacial Shear Stress

During the rubbing process, the shear force can reduce the activation energy barriers [65], so the tribochemical reaction should be easier at higher shear stress. The shear stress contours at the contact interface  $z = 0$  between the two rough surfaces (abbreviated as 'interfacial shear stress') at different temperatures and test durations are shown in Fig. 11.

As the test time increases, it is expected to see a larger deformation of the contact area along the rubbing direction as well as a decrease in the maximum value of the shear stress. As the temperature increases, the shear stress on the surface increases due to the increase in the friction coefficient. It is also found from FFO experiments and simulations that the tribofilm thickness increases with increasing temperature. Thus, it is consistent with the characteristic that the growth of ZDDP tribofilm is promoted by both stress and temperature [14-16].

**30 mins**

**180 mins**

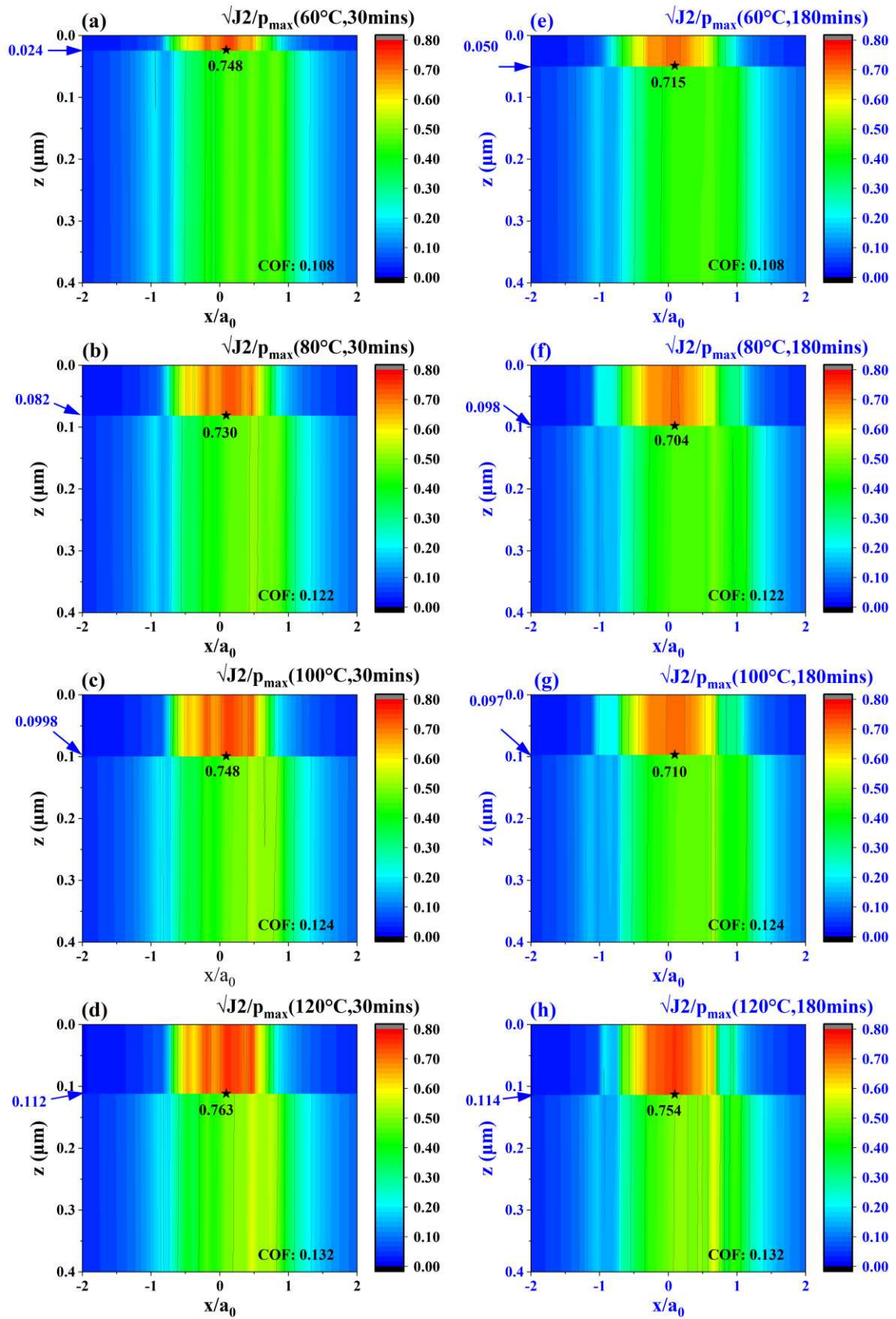


Fig. 10 Cross-section Von Mises stress contours ( $y = 0$ ) at different temperatures with the friction coefficient at the time steps equivalent to the 30 mins and 180 mins of experiments.

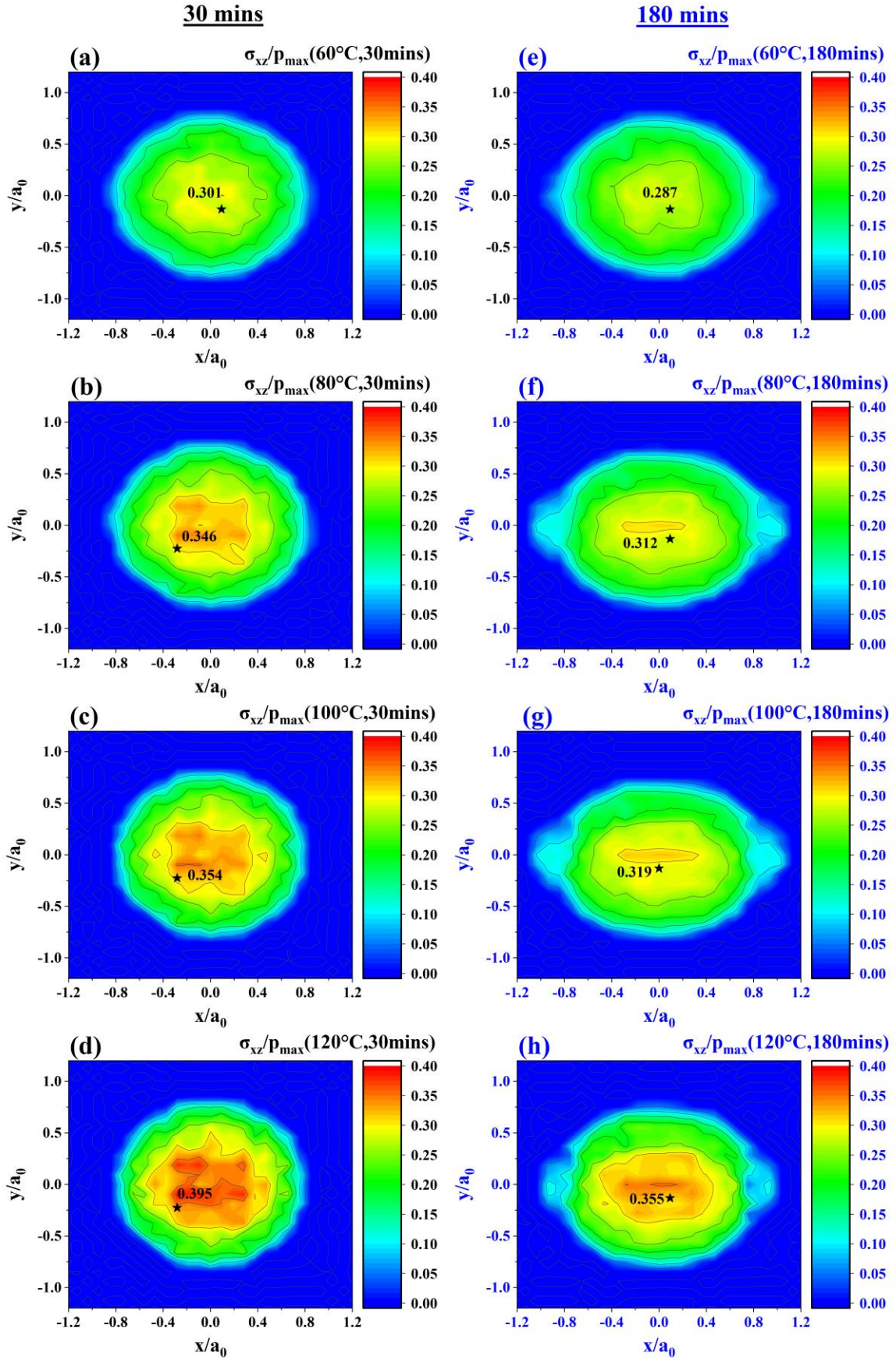


Fig. 11 Interfacial shear stress contours ( $z = 0$ ) at different temperatures with the friction coefficient at the time steps equivalent to the 30 mins and 180 mins of experiments.

### 4.3 Discussion

The primary purpose of this work is to develop a wear model involving the tribochemistry of FFO and to apply the layered contact model feature in which the layer's material properties can be modified to calculate the effect of the tribofilm thickness on the sublayer stress. However, because FFO has complex chemical formulations, its modelling work involves the participation of experimental results, making the parameters/constants used in the model have certain limitations. Therefore, this study focuses more on validating computational processes and improving the methodology rather than optimising the simulation accuracy. The validity of the key assumptions used in each part of the modelling framework is further discussed below, including the interactions with experimental data, simulation results, and comparisons with related research methods.

One of the layered contact model assumptions is the continuity of the layer material, but the tribofilm is usually patch-like. However, some studies have shown that ZDDP tribofilm is flowable under high pressure and shear stress [66, 67]. Therefore, it can be assumed that when two surfaces are in contact, the tribofilm on the surface and the lubricant molecules entrained form a mixture that is a viscous and flowable layer under shear. When tribofilm reaches a certain average thickness, it is reasonable to consider it a continuous layer covering the steel surface in contact. The average tribofilm thickness changes the layer thickness in each iteration.

For developing a tribochemistry model for FFO, it is difficult to discuss the reaction kinetic mechanisms or parameters under microscopic conditions like ZDDP due to the uniqueness and commercial confidentiality of additive formulations. It is not the first task for non-lubricant manufacturers to define tribochemical reaction paths or correlate variables in the model with parameters such as additive concentration. However, the tribofilm growth alters the surface topography and material properties and affects the contact between asperities, making the tribofilm thickness an indispensable parameter in the layered contact model. Therefore, since the growth curve and main chemical composition of the FFO tribofilm are similar to those of the ZDDP tribofilm, the tribochemical model of the ZDDP tribofilm developed by Ghanbarzadeh *et al.* [7, 13], which is also based on the MTM-SLIM experiments, was modified for FFO tribofilm. A hypothesis of reaction priority or intense competition between additives in FFO is proposed in part(I) of this research, which may lead to poor durability of the tribofilm in the initial formation, resulting in a time difference between the two growths or reaction paths. Hence, the tribochemistry model for FFO is the sum of two 'growth terms', which is different from ZDDP.

The tribofilm formation typically involves a balance of growth and removal. Fujita and Spikes [11, 68] used the dispersant to remove ZDDP tribofilm that had reached the stable phase and developed the removal part of the model. However, since FFO initially contains dispersant, it remains to be verified whether the same method can be performed on FFO tribofilm. Many researchers have also expressed the removal rate of the tribofilm by a coefficient related to the tribofilm thickness, which may be exponential [7] or linear [8], or the removal amount

is a constant [17]. In this study, the tribofilm growth curve used for fitting is derived from the combined effect of tribofilm growth and removal in experiments. Therefore, there is no explicit expression representing the tribofilm removal in the tribofilm formation equation. However, it does not mean that it has not been considered. In the wear model, the removal rate of the tribofilm is assumed to be constant.

The wear model is based on Archard's wear equation, which can easily correlate with experimental conditions such as load, stress, and sliding distance. In calculating the wear coefficient  $K$ , the idea of using Fe at.% in the XPS data proposed by Bosman and Schipper [6] was followed. Their contact model is based on a multi-level multi-summation algorithm [69], which uses the plastic strain on the tribofilm surface to express the wear. However, the wear test in this paper is the material loss on steel substrate after removing the tribofilm. The contact model is different, so the original method is unsuitable. According to the chemical analysis in Part (I), most of the iron in the tribofilm exists in iron sulphide or oxide forms, which is different from the density of iron in the substrate. Therefore, the principle of mass conservation is used to correlate the iron lost in the substrate with that in the removed tribofilm, introducing more physical meaning to the model.

Compared to conventional surface contact algorithms, this layered contact model can simulate the stress state under the influence of tribofilm material and roughness. For example, von Mises stress is the comprehensive stress commonly used in mechanics to calculate the strength of a material. It is used to evaluate whether the material yields, breaks, etc. The simulation results show that the maximum stress value occurs near the contact centre on the interface between the tribofilm and the steel substrate. The ratio of this value to the maximum Hertzian contact pressure is about 0.7~ 0.76 for all tested temperatures, indicating a reduced contact pressure on the surface of the steel substrate due to the relatively soft tribofilm, which is consistent with the tribofilms' mechanism of buffering and isolating the contact. Even when the tribofilm thickness is 20 nm, the stress value is significantly reduced.

According to the stress-activated Arrhenius thermal model, the increase in shear stress can reduce the activation energy of the ZDDP reaction [15, 65] so that ZDDP can easily generate tribofilm in sliding contact at normal working temperature. The same can also be applied to FFO containing ZDDP. The simulation results show that as the temperature increases, the shear stress on the surface of the FFO tribofilm increases. At the same temperature, the shear stress in the growth phase of the tribofilm is higher than that in the stable phase. In addition, as the test time increases, the contact area will be elongated along the sliding direction, which is also predictable. This also demonstrates the effectiveness of this method in analysing the contact pressure and shear stress under the influence of FFO tribofilm.

## 5 Conclusions

This paper developed a wear model involving the tribochemistry of FFO based on the layered contact model. The simulation results of the tribofilm growth and the wear evolution agree well with the experimental results. The main conclusions are summarised as follows.

- 1) The layered contact model is applied to simulate the sublayer stress under the influence of the real-time tribofilm growth for the first time. It extends the simulation flowchart based on asperity-asperity contact from the two-dimensional surface to the three-dimensional layered structure. Different material properties of the tribofilm and the substrate can be considered in the model.
- 2) A tribochemistry model and a wear model when using FFO are developed based on the modelling studies of ZDDP and the experimental results of FFO. Significantly, different chemical structures of iron in tribofilm and steel substrate are considered in the wear model, improving the physical meaning of the previous wear model for ZDDP.
- 3) Using the layered contact model for rough surfaces, the model successfully simulates that the formation of the tribofilm has a buffering effect on the contact, and the growth of the tribofilm is promoted by temperature and shear.

This model framework successfully attempts to model tribochemical and wear characteristics on contact surfaces when using FFO with complex chemical compositions under a boundary lubrication regime. It provides an approach for simulating tribochemistry, wear, and sublayer stress when using a general FFO with similar recipes and properties or other functional surfaces.

## References

1. Holmberg, K. and A. Erdemir, *Influence of tribology on global energy consumption, costs and emissions*. Friction, 2017. **5**(3): p. 263-284.
2. Holmberg, K., et al., *Global energy consumption due to friction and wear in the mining industry*. Tribology International, 2017. **115**: p. 116-139.
3. Bhushan, B., *Introduction to tribology*. 2013: John Wiley & Sons.
4. Bruce, R.W., *Handbook of Lubrication and Tribology, Volume II: Theory and Design, Second Edition*. 2012, Baton Rouge: CRC Press.
5. Holm, R., *Electric Contacts, Hugo Gebers*. Förlag (Stockholm, Sweden), 1946.
6. Bosman, R. and D.J. Schipper, *Mild wear prediction of boundary-lubricated contacts*. Tribology letters, 2011. **42**(2): p. 169-178.
7. Ghanbarzadeh, A., et al., *A semi-deterministic wear model considering the effect of zinc dialkyl dithiophosphate tribofilm*. Tribology Letters, 2016. **61**(1): p. 12.
8. Akchurin, A. and R. Bosman, *A Deterministic Stress-Activated Model for Tribo-Film Growth and Wear Simulation*. Tribology Letters, 2017. **65**(2): p. 59.
9. Gong, Y., et al., *Experimental and Numerical Study on Wear Characteristics of Steel Surfaces Involving the Tribochemistry of a Fully Formulated Oil Part I: Experiments*. Tribology International, 2022: p. 107888.
10. So, H. and Y.C. Lin, *The theory of antiwear for ZDDP at elevated temperature in boundary lubrication condition*. Wear, 1994. **177**(2): p. 105-115.
11. Fujita, H. and H.A. Spikes, *Study of Zinc Dialkyldithiophosphate Antiwear Film Formation and Removal Processes, Part II: Kinetic Model*. Tribology Transactions, 2005. **48**(4): p. 567-575.
12. Andersson, J., et al., *Semi-deterministic chemo-mechanical model of boundary lubrication*. Faraday discussions, 2012. **156**(1): p. 343-360.
13. Ghanbarzadeh, A., et al., *Development of a new mechano-chemical model in boundary lubrication*. Tribology International, 2016. **93**: p. 573-582.
14. Bulgarevich, S.B., et al., *Kinetics of mechanoactivation of tribochemical processes*. Journal of Friction and Wear, 2012. **33**(5): p. 345-353.
15. Gosvami, N., et al., *Mechanisms of antiwear tribofilm growth revealed in situ by single-asperity sliding contacts*. Science, 2015. **348**(6230): p. 102-106.
16. Dorgham, A., et al., *Single-asperity study of the reaction kinetics of P-based triboreactive films*. Tribology International, 2019. **133**: p. 288-296.
17. Domínguez-García, S., et al., *Mass balance of the tribofilm in lubricated systems*. Tribology International, 2021. **155**.
18. Bec, S., et al. *Relationship between mechanical properties and structures of zinc dithiophosphate anti-wear films*. in *Proceedings of the Royal Society of London A: Mathematical, Physical and Engineering Sciences*. 1999. The Royal Society.
19. Demmou, K., et al., *Temperature effects on mechanical properties of zinc dithiophosphate tribofilms*. Tribology International, 2006. **39**(12): p. 1558-1563.

20. Pereira, G., et al., *A variable temperature mechanical analysis of ZDDP-derived antiwear films formed on 52100 steel*. *Wear*, 2007. **262**(3): p. 461-470.
21. O'Sullivan, T.C. and R.B. King, *Sliding Contact Stress Field Due to a Spherical Indenter on a Layered Elastic Half-Space*. *Journal of Tribology*, 1988. **110**(2): p. 235-240.
22. Lainé, E., A. Olver, and T. Beveridge, *Effect of lubricants on micropitting and wear*. *Tribology International*, 2008. **41**(11): p. 1049-1055.
23. Brizmer, V., H. Pasaribu, and G.E. Morales-Espejel, *Micropitting performance of oil additives in lubricated rolling contacts*. *Tribology transactions*, 2013. **56**(5): p. 739-748.
24. Soltanahmadi, S., et al., *Investigation of the effect of a diamine-based friction modifier on micropitting and the properties of tribofilms in rolling-sliding contacts*. *Journal of Physics D: Applied Physics*, 2016. **49**(50): p. 505302.
25. Soltanahmadi, S., et al., *Tribochemical study of micropitting in tribocorrosive lubricated contacts: The influence of water and relative humidity*. *Tribology International*, 2017. **107**: p. 184-198.
26. Cen, H., A. Morina, and A. Neville, *Effect of slide to roll ratio on the micropitting behaviour in rolling-sliding contacts lubricated with ZDDP-containing lubricants*. *Tribology International*, 2018. **122**: p. 210-217.
27. Ueda, M., H. Spikes, and A. Kadiric, *In-situ observations of the effect of the ZDDP tribofilm growth on micropitting*. *Tribology International*, 2019. **138**: p. 342-352.
28. Burmister, D.M., *The General Theory of Stresses and Displacements in Layered Systems. I*. *Journal of Applied Physics*, 1945. **16**(2): p. 89-94.
29. Burmister, D.M., *The General Theory of Stresses and Displacements in Layered Soil Systems. II*. *Journal of Applied Physics*, 1945. **16**(3): p. 126-127.
30. Burmister, D.M., *The General Theory of Stresses and Displacements in Layered Soil Systems. III*. *Journal of Applied Physics*, 1945. **16**(5): p. 296-302.
31. Chen, W., *Computation of stresses and displacements in a layered elastic medium*. *International Journal of Engineering Science*, 1971. **9**(9): p. 775-800.
32. Chen, W. and P. Engel, *Impact and contact stress analysis in multilayer media*. *International Journal of Solids and Structures*, 1972. **8**(11): p. 1257-1281.
33. Komvopoulos, K., *Finite element analysis of a layered elastic solid in normal contact with a rigid surface*. 1988.
34. Komvopoulos, K., *Elastic-plastic finite element analysis of indented layered media*. 1989.
35. Diao, D., K. Kato, and K. Hayashi, *The maximum tensile stress on a hard coating under sliding friction*. *Tribology International*, 1994. **27**(4): p. 267-272.
36. Kral, E. and K. Komvopoulos, *Three-dimensional finite element analysis of surface deformation and stresses in an elastic-plastic layered medium subjected to indentation and sliding contact loading*. 1996.
37. Stephens, L., Y. Liu, and E. Meletis, *Finite element analysis of the initial yielding behavior of a hard coating/substrate system with functionally graded interface under indentation and friction*. *J. Trib.*, 2000. **122**(2): p. 381-387.
38. Kot, M., et al., *Analysis of spherical indentations of coating-substrate systems: experiments and finite element modeling*. *Materials & Design*, 2013. **43**: p. 99-111.

39. GUPTA, P.K. and J.A. WALOWIT, *Contact Stresses Between an Elastic Cylinder and a Layered Elastic Solid*. ASME, 1974. **96**: p. 250-257.
40. Cole, S.J. and R.S. Sayles, *A Numerical Model for the Contact of Layered Elastic Bodies With Real Rough Surfaces*. Journal of Tribology, 1992. **114**(2): p. 334-340.
41. Peng, W. and B. Bhushan, *A Numerical Three-Dimensional Model for the Contact of Layered Elastic/Plastic Solids With Rough Surfaces by a Variational Principle*. Journal of Tribology, 2001. **123**(2): p. 330.
42. Peng, W. and B. Bhushan, *Sliding Contact Analysis of Layered Elastic/Plastic Solids With Rough Surfaces*. Journal of Tribology, 2001. **124**(1): p. 46-61.
43. Peng, W. and B. Bhushan, *Transient analysis of sliding contact of layered elastic/plastic solids with rough surfaces*. Microsystem Technologies, 2003. **9**(5): p. 340-345.
44. Nogi, T. and T. Kato, *Influence of a Hard Surface Layer on the Limit of Elastic Contact—Part I: Analysis Using a Real Surface Model*. Journal of Tribology, 1997. **119**(3): p. 493-500.
45. Yu, C., Z. Wang, and Q.J. Wang, *Analytical frequency response functions for contact of multilayered materials*. Mechanics of Materials, 2014. **76**: p. 102-120.
46. Nyqvist, J., et al., *Semi-analytical model for rough multilayered contacts*. Tribology International, 2015. **87**: p. 98-112.
47. Tian, X. and B. Bhushan, *A numerical three-dimensional model for the contact of rough surfaces by variational principle*. Journal of tribology, 1996. **118**(1): p. 33-42.
48. Hashin, Z., *Thermoelastic properties of fiber composites with imperfect interface*. Mechanics of Materials, 1990. **8**(4): p. 333-348.
49. Qu, J., *The effect of slightly weakened interfaces on the overall elastic properties of composite materials*. Mechanics of Materials, 1993. **14**(4): p. 269-281.
50. Yu, H.Y., *A new dislocation-like model for imperfect interfaces and their effect on load transfer*. Composites Part A: Applied Science and Manufacturing, 1998. **29**(9): p. 1057-1062.
51. Yu, H., Y. Wei, and F. Chiang, *Load transfer at imperfect interfaces—dislocation-like model*. International journal of engineering science, 2002. **40**(14): p. 1647-1662.
52. Pan, E., *Three-dimensional Green's functions in anisotropic elastic bimaterials with imperfect interfaces*. J. Appl. Mech., 2003. **70**(2): p. 180-190.
53. Benveniste, Y. and T. Chen, *On the Saint-Venant torsion of composite bars with imperfect interfaces*. Proceedings of the Royal Society of London. Series A: Mathematical, Physical and Engineering Sciences, 2001. **457**(2005): p. 231-255.
54. Yu, H. and S. Sanday, *Elastic fields in joined half-spaces due to nuclei of strain*. Proceedings of the Royal Society of London. Series A: Mathematical and Physical Sciences, 1991. **434**(1892): p. 503-519.
55. Yu, H., Z. Wang, and Q. Wang, *Analytical solutions for the elastic fields caused by eigenstrains in two frictionlessly joined half-spaces*. International Journal of Solids and Structures, 2016. **100-101**: p. 74-94.
56. Johnson, K.L., *Contact Mechanics*. 1987: Cambridge university press.
57. Liu, S., Q. Wang, and G. Liu, *A versatile method of discrete convolution and FFT (DC-FFT) for contact analyses*. Wear, 2000. **243**(1-2): p. 101-111.

58. Liu, S. and Q. Wang, *Studying Contact Stress Fields Caused by Surface Traction With a Discrete Convolution and Fast Fourier Transform Algorithm*. Journal of Tribology, 2002. **124**(1): p. 36-45.
59. Yu, C., et al., *Maximum von Mises Stress and Its Location in Trilayer Materials in Contact*. Journal of Tribology, 2016. **138**(4).
60. Stanley, H. and T. Kato, *An FFT-based method for rough surface contact*. Journal of tribology, 1997. **119**(3): p. 481-485.
61. Almqvist, A., et al., *On the dry elasto-plastic contact of nominally flat surfaces*. Tribology international, 2007. **40**(4): p. 574-579.
62. Wang, Y., Y. Liu, and Y. Wang. *A method for improving the capability of convergence of numerical lubrication simulation by using the PID controller*. in *IFTOMM World Congress on Mechanism and Machine Science*. 2019. Springer.
63. Kato, K., *3 - Friction and wear of passive metals and coatings*, in *Tribocorrosion of Passive Metals and Coatings*, D. Landolt and S. Mischler, Editors. 2011, Woodhead Publishing. p. 65-99.
64. Hu, Y.Z. and K. Tonder, *Simulation of 3-D Random Rough-Surface by 2-D Digital-Filter and Fourier-Analysis*. International Journal of Machine Tools & Manufacture, 1992. **32**(1-2): p. 83-90.
65. Zhang, J. and H. Spikes, *On the mechanism of ZDDP antiwear film formation*. Tribology Letters, 2016. **63**(2): p. 24.
66. Dorgham, A.K.Y., *Reaction kinetics and rheological characteristics of ultra-thin P-based triboreactive films*. 2017, University of Leeds.
67. Dorgham, A., et al., *LOCAL OCCUPANCY OF VISCOELASTIC INTERFACES: A NEW RHEOLOGICAL PERSPECTIVE ON ANTIWEAR TRIBOFILMS*. 2017.
68. Fujita, H., R. Glovnea, and H. Spikes, *Study of zinc dialkydithiophosphate antiwear film formation and removal processes, part I: experimental*. Tribology transactions, 2005. **48**(4): p. 558-566.
69. Polonsky, I. and L. Keer, *A numerical method for solving rough contact problems based on the multi-level multi-summation and conjugate gradient techniques*. Wear, 1999. **231**(2): p. 206-219.

## Appendix A Solutions of the Frequency Response Functions (FRFs)

O'Sullivan and King [21] used the Papkovitch-Neuber ( $P-N$ ) elastic potentials  $\phi_0$  and  $\vec{\phi}=(\phi_1, \phi_2, \phi_3)$ , which are the  $x, y, z$  components of the harmonic functions for zero body forces to express the deformation and stress as follows.

$$u_i = \frac{1}{2G} (\phi_{0,i} + x \cdot \phi_{1,i} + z \cdot \phi_{3,i} - (3-4\nu)\phi_i)$$

(A-1)

$$\sigma_{ij} = \phi_{0,ij} + x\phi_{1,ij} + z\phi_{3,ij} - 2\nu(\phi_{1,1} + \phi_{3,3})\delta_{ij} - (1-2\nu)(\phi_{i,j} + \phi_{j,i})$$

where  $G$  is the shear modulus;  $\nu$  is the Poisson's ratio; the index of  $i$  and  $j$  are 1, 2, 3 corresponding to  $x, y, z$ ,

respectively;  $\delta_{ij}$  is Kronecker delta:  $\delta_{ij} = \begin{cases} 1 & i = j \\ 0 & i \neq j \end{cases}$ .

Since the Fourier transform decomposes the harmonic function into the sinusoidal waveform at different frequencies, the superposition of these sine curves is also a harmonic function. In the frequency domain, the expressions of the transformed  $P-N$  potentials in the layer and the substrate are:

$$\text{layer: } \begin{cases} \Phi_0^{(1)} = A^{(1)}e^{-\alpha z_1} + \bar{A}^{(1)}e^{\alpha z_1} \\ \Phi_1^{(1)} = B^{(1)}e^{-\alpha z_1} + \bar{B}^{(1)}e^{\alpha z_1} \\ \Phi_3^{(1)} = C^{(1)}e^{-\alpha z_1} + \bar{C}^{(1)}e^{\alpha z_1} \end{cases} \quad \text{and Substrate: } \begin{cases} \Phi_0^{(2)} = A^{(2)}e^{-\alpha z_1} \\ \Phi_1^{(2)} = B^{(2)}e^{-\alpha z_1} \\ \Phi_3^{(2)} = C^{(2)}e^{-\alpha z_1} \end{cases} \quad (\text{A-2})$$

where the line on  $A, B$  and  $C$  indicate their corresponding complex conjugates,  $\alpha = \sqrt{m^2 + n^2}$ , where  $m$  and  $n$  correspond to the frequency variables of  $x$  and  $y$  in the frequency domain after Fourier transform. Since the assumptions of an infinite depth of the contact body, both stress and deformation are zero so  $\bar{A}^{(2)} = \bar{B}^{(2)} = \bar{C}^{(2)} = 0$  which has been eliminated in the Equ.(A-2).

The normal pressure is set to be 1 at the centre of the origin, accompanied by shear stress, that is  $p(0,0,0)=1, q(0,0,0)=\mu$ . The boundary conditions at the layer surface  $z=0$  are:

$$\begin{cases} \sigma_{zz}^{(1)}(x, y, 0) = -p(x, y, 0) = \begin{cases} -1 & x=0, y=0 \\ 0 & x \neq 0, y \neq 0 \end{cases} \\ \sigma_{xz}^{(1)}(x, y, 0) = \mu p(x, y, 0) = \begin{cases} \mu & x=0, y=0 \\ 0 & x \neq 0, y \neq 0 \end{cases} \\ \sigma_{yz}^{(1)}(x, y, 0) = 0 \end{cases} \quad (\text{A-3})$$

Assuming that the layer is fully bonded to the substrate, so both stress and deformation on the interface of the layer and the substrate are continuous. On the interface, the boundary conditions are:

$$\begin{cases} \sigma_{xz}^{(1)}(x, y, h) = \sigma_{xz}^{(2)}(x, y, 0) \\ \sigma_{yz}^{(1)}(x, y, h) = \sigma_{yz}^{(2)}(x, y, 0) \\ \sigma_{zz}^{(1)}(x, y, h) = \sigma_{zz}^{(2)}(x, y, 0) \end{cases} \text{ and } \begin{cases} u_x^{(1)}(x, y, h) = u_x^{(2)}(x, y, 0) \\ u_y^{(1)}(x, y, h) = u_y^{(2)}(x, y, 0) \\ u_z^{(1)}(x, y, h) = u_z^{(2)}(x, y, 0) \end{cases} \quad (\text{A-4})$$

where  $h$  is the layer thickness; (1) and (2) represent the layer and the substrate, respectively.

On the substrate, the stress and the deformation decrease to zero at a far depth from the surface.

$$\begin{cases} \sigma^{(2)}(x, y, \infty) = 0 \\ u^{(2)}(x, y, \infty) = 0 \end{cases} \quad (\text{A-5})$$

By substituting  $P$ - $N$  potentials into Equ.(A-1), then solving the equation sets Equ. (A-3)~(A-5), the deformation ( $u$ ) and stress ( $\sigma$ ) components of FRFs are shown in Equ. (A-6) and Equ.(A-7), respectively.

$$\begin{aligned} \hat{u}_x^{(j)} &= \frac{1}{2G_j} \left\{ im \left[ A^{(j)} e^{-\alpha z_j} + \bar{A}^{(j)} e^{\alpha z_j} \right] - 4(1-\nu_j) \left[ B^{(j)} e^{-\alpha z_j} + \bar{B}^{(j)} e^{\alpha z_j} \right] \right. \\ &\quad \left. + m^2 \alpha^{-1} z_j \left[ B^{(j)} e^{-\alpha z_j} - \bar{B}^{(j)} e^{\alpha z_j} \right] + im z_j \left[ C^{(j)} e^{-\alpha z_j} + \bar{C}^{(j)} e^{\alpha z_j} \right] - m \left[ B_{,m}^{(j)} e^{-\alpha z_j} + \bar{B}_{,m}^{(j)} e^{\alpha z_j} \right] \right\} \\ \hat{u}_y^{(j)} &= \frac{1}{2G_j} \left\{ in \left[ A^{(j)} e^{-\alpha z_j} + \bar{A}^{(j)} e^{\alpha z_j} \right] + mn \alpha^{-1} z_j \left[ B^{(j)} e^{-\alpha z_j} - \bar{B}^{(j)} e^{\alpha z_j} \right] \right. \\ &\quad \left. + in z_j \left[ C^{(j)} e^{-\alpha z_j} + \bar{C}^{(j)} e^{\alpha z_j} \right] - n \left[ B_{,m}^{(j)} e^{-\alpha z_j} + \bar{B}_{,m}^{(j)} e^{\alpha z_j} \right] \right\} \\ \hat{u}_z^{(j)} &= \frac{1}{2G_j} \left\{ -\alpha \left[ A^{(j)} e^{-\alpha z_j} - \bar{A}^{(j)} e^{\alpha z_j} \right] + im z_j \left[ B^{(j)} e^{-\alpha z_j} + \bar{B}^{(j)} e^{\alpha z_j} \right] - im \alpha^{-1} \left[ B^{(j)} e^{-\alpha z_j} - \bar{B}^{(j)} e^{\alpha z_j} \right] \right. \\ &\quad \left. - (3-4\nu_j) \left[ C^{(j)} e^{-\alpha z_j} + \bar{C}^{(j)} e^{\alpha z_j} \right] - \alpha z_j \left[ C^{(j)} e^{-\alpha z_j} - \bar{C}^{(j)} e^{\alpha z_j} \right] - i \alpha \left[ B_{,m}^{(j)} e^{-\alpha z_j} - \bar{B}_{,m}^{(j)} e^{\alpha z_j} \right] \right\} \end{aligned} \quad (\text{A-6})$$

$$\begin{aligned}
\hat{\sigma}_{xx}^{(j)} &= -m^2 \left[ A^{(j)} e^{-\alpha z_j} + \bar{A}^{(j)} e^{\alpha z_j} \right] + 2im(v_j - 2) \left[ B^{(j)} e^{-\alpha z_j} + \bar{B}^{(j)} e^{\alpha z_j} \right] + im^3 \alpha^{-1} z_j \left[ B^{(j)} e^{-\alpha z_j} - \bar{B}^{(j)} e^{\alpha z_j} \right] \\
&\quad - m^2 z_j \left[ C^{(j)} e^{-\alpha z_j} + \bar{C}^{(j)} e^{\alpha z_j} \right] + 2\alpha v_j \left[ C^{(j)} e^{-\alpha z_j} - \bar{C}^{(j)} e^{\alpha z_j} \right] - im^2 \left[ B_{,m}^{(j)} e^{-\alpha z_j} + \bar{B}_{,m}^{(j)} e^{\alpha z_j} \right] \\
\hat{\sigma}_{yy}^{(j)} &= -n^2 \left[ A^{(j)} e^{-\alpha z_j} + \bar{A}^{(j)} e^{\alpha z_j} \right] - 2imv_j \left[ B^{(j)} e^{-\alpha z_j} + \bar{B}^{(j)} e^{\alpha z_j} \right] + im^2 n \alpha^{-1} z_j \left[ B^{(j)} e^{-\alpha z_j} - \bar{B}^{(j)} e^{\alpha z_j} \right] \\
&\quad - n^2 z_j \left[ C^{(j)} e^{-\alpha z_j} + \bar{C}^{(j)} e^{\alpha z_j} \right] + 2\alpha v_j \left[ C^{(j)} e^{-\alpha z_j} - \bar{C}^{(j)} e^{\alpha z_j} \right] - in^2 \left[ B_{,m}^{(j)} e^{-\alpha z_j} + \bar{B}_{,m}^{(j)} e^{\alpha z_j} \right] \\
\hat{\sigma}_{zz}^{(j)} &= -\alpha^2 \left[ A^{(j)} e^{-\alpha z_j} + \bar{A}^{(j)} e^{\alpha z_j} \right] + 2im(1 - v_j) \left[ B^{(j)} e^{-\alpha z_j} + \bar{B}^{(j)} e^{\alpha z_j} \right] - im\alpha z_j \left[ B^{(j)} e^{-\alpha z_j} - \bar{B}^{(j)} e^{\alpha z_j} \right] \\
&\quad - \alpha^2 z_j \left[ C^{(j)} e^{-\alpha z_j} + \bar{C}^{(j)} e^{\alpha z_j} \right] + 2\alpha(1 - v_j) \left[ C^{(j)} e^{-\alpha z_j} - \bar{C}^{(j)} e^{\alpha z_j} \right] + i\alpha^2 \left[ B_{,m}^{(j)} e^{-\alpha z_j} + \bar{B}_{,m}^{(j)} e^{\alpha z_j} \right] \\
\hat{\sigma}_{xy}^{(j)} &= -mn \left[ A^{(j)} e^{-\alpha z_j} + \bar{A}^{(j)} e^{\alpha z_j} \right] - 2in(1 - v_j) \left[ B^{(j)} e^{-\alpha z_j} + \bar{B}^{(j)} e^{\alpha z_j} \right] + im^2 n \alpha^{-1} z_j \left[ B^{(j)} e^{-\alpha z_j} - \bar{B}^{(j)} e^{\alpha z_j} \right] \\
&\quad - mn z_j \left[ C^{(j)} e^{-\alpha z_j} + \bar{C}^{(j)} e^{\alpha z_j} \right] - inm \left[ B_{,m}^{(j)} e^{-\alpha z_j} + \bar{B}_{,m}^{(j)} e^{\alpha z_j} \right] \\
\hat{\sigma}_{xz}^{(j)} &= -im\alpha \left[ A^{(j)} e^{-\alpha z_j} - \bar{A}^{(j)} e^{\alpha z_j} \right] - m^2 z_j \left[ B^{(j)} e^{-\alpha z_j} + \bar{B}^{(j)} e^{\alpha z_j} \right] + \left[ 2\alpha(1 - v_j) + m^2 \alpha^{-1} \right] \left[ B^{(j)} e^{-\alpha z_j} - \bar{B}^{(j)} e^{\alpha z_j} \right] \\
&\quad - im(1 - 2v_j) \left[ C^{(j)} e^{-\alpha z_j} + \bar{C}^{(j)} e^{\alpha z_j} \right] - im\alpha z_j \left[ C^{(j)} e^{-\alpha z_j} - \bar{C}^{(j)} e^{\alpha z_j} \right] + m\alpha \left[ B_{,m}^{(j)} e^{-\alpha z_j} - \bar{B}_{,m}^{(j)} e^{\alpha z_j} \right] \\
\hat{\sigma}_{yz}^{(j)} &= -in\alpha \left[ A^{(j)} e^{-\alpha z_j} - \bar{A}^{(j)} e^{\alpha z_j} \right] - mn z_j \left[ B^{(j)} e^{-\alpha z_j} + \bar{B}^{(j)} e^{\alpha z_j} \right] + mn\alpha^{-1} \left[ B^{(j)} e^{-\alpha z_j} - \bar{B}^{(j)} e^{\alpha z_j} \right] \\
&\quad - in(1 - 2v_j) \left[ C^{(j)} e^{-\alpha z_j} + \bar{C}^{(j)} e^{\alpha z_j} \right] - in\alpha z_j \left[ C^{(j)} e^{-\alpha z_j} - \bar{C}^{(j)} e^{\alpha z_j} \right] + n\alpha \left[ B_{,m}^{(j)} e^{-\alpha z_j} - \bar{B}_{,m}^{(j)} e^{\alpha z_j} \right]
\end{aligned} \tag{A-7}$$

where  $\alpha = \sqrt{m^2 + n^2}$  in which  $m$  and  $n$  correspond to the frequency variables of  $x$  and  $y$  in the frequency domain after Fourier transform; The index  $j$  is 1 or 2 representing the layer or the substrate, respectively;  $i$  is the imaginary unit;  $z$  is the depth;  $\nu$  is the Poisson's ratio. The expressions of the nine parameters  $A^{(1)}$ ,  $\bar{A}^{(1)}$ ,  $B^{(1)}$ ,  $\bar{B}^{(1)}$ ,  $C^{(1)}$ ,  $\bar{C}^{(1)}$ ,  $A^{(2)}$ ,  $B^{(2)}$  and  $C^{(2)}$  are expressed below.

Due to the 3 parameters  $B^{(1)}$ ,  $\bar{B}^{(1)}$ , and  $B^{(2)}$  only related to tangential force, they can be calculated separately at first.

$$\begin{aligned}
\bar{B}^{(1)} &= - \left[ \frac{(G-1)e^{-2ah}}{(1+G) + (1-G)e^{-2ah}} \right] \frac{\bar{q}(m, n, 0)}{2\alpha(1-\nu_1)} \\
B^{(1)} &= \bar{B}^{(1)} - \frac{\bar{q}(m, n)}{2\alpha(1-\nu_1)} \\
B^{(2)} &= -2 \left( \frac{1-\nu_1}{1-\nu_2} \right) \left[ \frac{e^{-2ah}}{(1+\mu) + (1-\mu)e^{-2ah}} \right] \frac{\bar{q}(m, n, 0)}{2\alpha(1-\nu_1)}
\end{aligned} \tag{A-8}$$

where  $G = G_1 / G_2$ ,  $G_1 = \frac{E_1}{2(1+\nu_1)}$  and  $G_2 = \frac{E_2}{2(1+\nu_2)}$  are the shear modulus of layer and substrate, respectively;

$E$  and  $\nu$  are the elastic modulus and Poisson's ratio, respectively; The index 1 or 2 represents the layer or the

substrate, respectively;  $\bar{q}(m,n,0) = \mu\bar{p}(m,n,0)$  and  $\mu$  is friction coefficient;  $\bar{p}(m,n,0)$  is the Fourier transform of pressure  $p(x,y,0)$  and equals to 1 everywhere.

The expressions for the remaining 6 parameters related to terms  $A$  and  $C$  are shown in the Equ.(A-9).

$$\begin{aligned}
\langle \alpha^2 R_1 \rangle &= \alpha^2 (A^{(1)} - \bar{A}^{(1)}) + \alpha(1-2\nu_1)(C^{(1)} + \bar{C}^{(1)}) \\
\langle \alpha^2 R_2 \rangle &= \alpha^2 (A^{(1)} + \bar{A}^{(1)}) - 2\alpha(1-\nu_1)(\bar{C}^{(1)} - C^{(1)}) \\
\langle \alpha^2 R_3 \rangle &= \alpha \left[ \begin{aligned} &\alpha A^{(1)} - \alpha \bar{A}^{(1)} e^{2\alpha h} + ((1-2\nu_1) + \alpha h)C^{(1)} + ((1-2\nu_1) - \alpha h)e^{2\alpha h}\bar{C}^{(1)} \\ &- \alpha e^{\alpha h} A^{(2)} - (1-2\nu_2)e^{\alpha h} C^{(2)} \end{aligned} \right] \\
\langle \alpha^2 R_4 \rangle &= \alpha \left[ \begin{aligned} &\alpha A^{(1)} + \alpha e^{2\alpha h} \bar{A}^{(1)} - \alpha e^{\alpha h} A^{(2)} + (\alpha h + 2(1-\nu_1))C^{(1)} \\ &+ (\alpha h - 2(1-\nu_1))e^{2\alpha h}\bar{C}^{(1)} - 2(1-\nu_2)e^{\alpha h} C^{(2)} \end{aligned} \right] \\
\langle \alpha^2 R_5 \rangle &= \alpha \left[ \alpha A^{(1)} + \alpha e^{2\alpha h} \bar{A}^{(1)} + \alpha h C^{(1)} + \alpha h e^{2\alpha h} \bar{C}^{(1)} - G\alpha e^{\alpha h} A^{(2)} \right] \\
\langle \alpha^2 R_6 \rangle &= \alpha \left[ \begin{aligned} &\alpha A^{(1)} - \alpha e^{2\alpha h} \bar{A}^{(1)} + (\alpha h + (3-4\nu_1))C^{(1)} - (\alpha h - (3-4\nu_1))e^{2\alpha h}\bar{C}^{(1)} \\ &- \alpha G e^{\alpha h} A^{(2)} - (3-4\nu_2)G e^{\alpha h} C^{(2)} \end{aligned} \right]
\end{aligned} \tag{A-9}$$

The terms  $\lambda$ ,  $k$ ,  $\theta$  and  $S_0$  are set to satisfy:

$$\begin{aligned}
\lambda &= 1 - \frac{4(1-\nu_1)}{1 + \mu(3-4\nu_2)}, \quad k = \frac{\mu-1}{\mu + (3-4\nu_1)}, \quad \theta = e^{2\alpha h} \\
S_0 &= [\mu + (3-4\nu_1)] [1 - k e^{-2\alpha h}] = [\mu + (3-4\nu_1)] \left[ 1 - \frac{k}{\theta} \right]
\end{aligned} \tag{A-10}$$

Then, the solutions of the 6 unknown parameters in the equation set (A-9) are:

$$\begin{aligned}
C^{(1)} &= \frac{(1-\lambda)kS_0 R_c}{4(1-\nu_1)(\mu-1)[(\lambda/\theta-1)(k/\theta-1) - 4\alpha^2 h^2 k/\theta]} \\
\bar{C}^{(1)} &= \frac{2\alpha h(1/\theta)C^{(1)} + (1/\theta)R_a}{S_0} \\
A^{(1)} &= \frac{1}{2\alpha} [-(3-4\nu_1)C^{(1)} + \bar{C}^{(1)} + \alpha(R_1 + R_2)] \\
\bar{A}^{(1)} &= \frac{1}{2\alpha} (-C^{(1)} + (3-4\nu_1)\bar{C}^{(1)} - \alpha(R_1 - R_2)) \\
C^{(2)} &= \frac{(1-\lambda)\alpha/\sqrt{\theta}}{4(1-\nu_1)} (R_3 - R_4 + R_5 - R_6) + (1-\lambda)C^{(1)}/\sqrt{\theta} \\
A^{(2)} &= -\frac{h\theta(1-k)}{\sqrt{\theta}(k-\theta)} C^{(1)} - \frac{(3-4\nu_2)}{2\alpha} C^{(2)} + \frac{[R_1 + R_2 - (R_3 + R_4)]}{2\sqrt{\theta}} + \frac{(1/\theta)R_a}{2S_0} \left( \frac{1-\theta}{\alpha\sqrt{\theta}} \right)
\end{aligned} \tag{A-11}$$

where

$$R_a = \alpha [(\mu - 1)(R_1 + R_2) - \mu(R_3 + R_4) + (R_5 + R_6)]$$

$$R_b = \alpha \left[ (R_2 - R_1) + (R_3 - R_4)/\theta - \frac{(1 - \lambda)}{4\theta(1 - \nu_1)} [(R_3 - R_4) + (R_5 - R_6)] \right]$$

$$R_c = \frac{4(1 - \nu_1)}{1 - \lambda} \left( \frac{2\alpha h R_a / \theta}{S_0} + R_b \right)$$